Intelligent Pharmacy 4 (2026) 67–87

Contents lists available at ScienceDirect

Intelligent Pharmacy

journal homepage: www.keaipublishing.com/en/journals/intelligent-pharmacy

Full length article

Network pharmacology and molecular simulation-based analysis of *Citrus aurantium* metabolites targeting breast cancer pathways

Taufik Muhammad Fakih[a,b], Haura Syabihah[b], Tri Awalani Sapa'ati Gusti[b], Tifanil Oktafira[b], Nency Oktavia Sri Mulyani[b], Hilda Aprilia Wisnuwardhani[b], Muchtaridi Muchtaridi[a,c,*]

[a] *Department of Pharmaceutical Analysis and Medicinal Chemistry, Faculty of Pharmacy, Universitas Padjadjaran, Jl. Raya Bandung-Sumedang, Sumedang, 45363, Indonesia*

[b] *Department of Pharmacy, Faculty of Mathematics and Natural Sciences, Universitas Islam Bandung, Jl. Ranggagading, Bandung, 40116, Indonesia*

[c] *Research Collaboration Centre for Radiopharmaceuticals Theranostic, National Research and Innovation Agency (BRIN), Jl. Raya Bandung-Sumedang, Sumedang, 45363, Indonesia*

ARTICLE INFO

Keywords:
Natural compounds
Citrus aurantium
Network pharmacology
Estrogen receptor 1 (ESR1)
Breast cancer therapy
Computational approach

ABSTRACT

Citrus aurantium is a plant known for its diverse bioactive constituents, yet its therapeutic potential in hormone-dependent breast cancer remains underexplored. This study applied a network pharmacology approach to identify breast cancer-associated targets, followed by molecular docking, molecular dynamics simulation, and MM-PBSA energy analysis to evaluate ligand–receptor interactions. From an initial dataset of 111 metabolites, 24 compounds were predicted to interact with ESR1, a central node identified through protein–protein interaction network analysis. Several flavonoid derivatives demonstrated favorable docking interactions at key ESR1 residues, including GLU353, ALA350, LEU387, ARG394, LYS449, and PRO324. Molecular dynamics simulations up to 300 ns revealed that the native ligand complex maintained the greatest stability, 5,7,3′,4′-tetrahydroxyflavone achieved persistent receptor engagement with moderate flexibility, and hesperetin showed higher deviations yet equilibrated with selective residue interactions. MM-PBSA binding free energy calculations confirmed that 5,7,3′,4′-tetrahydroxyflavone possessed the strongest affinity (−79.695 kJ/mol), followed by the native ligand (−72.521 kJ/mol), while hesperetin displayed weaker but still favorable binding (−55.737 kJ/mol). These energetic contributions were largely driven by van der Waals and electrostatic forces, partially offset by polar solvation. The integrated computational findings highlight 5,7,3′,4′-tetrahydroxyflavone as the most promising ESR1 binder from *Citrus aurantium*, while hesperetin remains a viable candidate through its selective pharmacophoric interactions. Collectively, these findings establish a solid foundation for subsequent experimental validation and support the development of *Citrus aurantium*-derived compounds as potential therapies for estrogen receptor-positive breast cancer.

1. Introduction

Breast cancer is the most frequently diagnosed malignancy among women and ranks among the top three most common cancers globally, alongside lung and colorectal cancer.[1,2] It primarily affects women, with risk increasing substantially with age; more than 80% of cases occur in women aged 50 years and older.[3] In 2020 alone, breast cancer was responsible for approximately 685,000 deaths worldwide, making it the leading cause of cancer-related mortality in women.[4] Therapeutic regimens such as tamoxifen and doxorubicin have contributed significantly to clinical management but are associated with considerable side effects, including cardiotoxicity and endocrine dysfunction.[5] Alarmingly, Asia experienced the highest rise in breast cancer prevalence in 2022, accounting for 39.1% of all new global cases.[6] Current frontline pharmacological therapies include agents such as doxorubicin, trastuzumab, tamoxifen, paclitaxel, pembrolizumab, and everolimus.[7] Despite their efficacy, these treatments frequently result in adverse outcomes that compromise patient quality of life and limit long-term adherence.[8] Consequently, there is an urgent need to discover novel therapeutic strategies that offer both safety and efficacy. In this context, natural

* Corresponding author. Department of Pharmaceutical Analysis and Medicinal Chemistry, Faculty of Pharmacy, Universitas Padjadjaran, Jl. Raya Bandung-Sumedang, Sumedang, 45363, Indonesia.
E-mail address: muchtaridi@unpad.ac.id (M. Muchtaridi).

Peer review under the responsibility of Editorial Board of Intelligent Pharmacy.

https://doi.org/10.1016/j.ipha.2025.11.001
Received 25 September 2025; Received in revised form 31 October 2025; Accepted 3 November 2025
Available online 4 November 2025
2949-866X/© 2026 Publishing services by Elsevier B.V. on behalf of Higher Education Press and KeAi Communications Co. Ltd. This is an open access article under the CC BY license (http://creativecommons.org/licenses/by/4.0/).

products derived from medicinal plants have emerged as promising alternatives due to their multitarget actions and lower toxicity profiles. The exploration of plant-derived compounds presents a valuable opportunity to address the shortcomings of existing cancer treatments.

Indonesia is home to a rich biodiversity of medicinal plants that have long been used in traditional herbal remedies. These indigenous botanicals hold untapped potential as sources of bioactive compounds that may complement or substitute existing cancer therapies.[9,10] With increasing interest in non-toxic, sustainable, and culturally integrated treatment options, the exploration of Indonesia's natural products has gained momentum in both local and international scientific communities.[11] Herbal medicines, in particular, are gaining popularity among patients seeking gentler therapeutic alternatives to conventional chemotherapy and targeted treatments. The development of phytomedicines from native plants offers several advantages, including accessibility, cost-effectiveness, and ecological sustainability.[12,13] Furthermore, these approaches can support the growth of Indonesia's health and biopharmaceutical industries. As scientific validation becomes more integrated with ethnobotanical knowledge, many plant species traditionally used in folk medicine are being subjected to modern pharmacological scrutiny.[14] Identifying specific mechanisms of action through computational and molecular techniques enhances the credibility of such therapies. Accordingly, there is growing interest in investigating locally available herbs with reported anticancer effects, especially for high-burden diseases like breast cancer.

Citrus aurantium, also known as bitter orange, is a plant species from the Rutaceae family that has garnered attention for its diverse pharmacological activities.[15] Native to Southeast Asia, this plant is now widely cultivated in various regions, including North Africa, the Middle East, and Europe.[16] Its fruits are edible, but its peels, flowers, seeds, and leaves are particularly valued for their rich content of bioactive compounds such as flavonoids, alkaloids, and essential oils.[17] Numerous studies have reported the therapeutic potential of *Citrus aurantium* derivatives, including their antibacterial, antifungal, anxiolytic, anti-obesity, hypoglycemic, and antioxidant properties. Importantly, several constituents, such as naringin, hesperidin, and nobiletin, have demonstrated cytotoxic activity against cancer cell lines and modulate key oncogenic pathways.[18,19] These phytochemicals are believed to exert effects on molecular targets related to proliferation, apoptosis, angiogenesis, and inflammation. Their multitarget nature makes them attractive candidates for diseases with complex pathologies such as cancer.[20] Moreover, the relatively low toxicity of these compounds enhances their potential for long-term therapeutic use. Despite promising preclinical data, the precise molecular mechanisms through which *Citrus aurantium* metabolites act against breast cancer remain underexplored.

To uncover the potential mechanisms underlying the anticancer effects of natural compounds, researchers increasingly rely on systems-level computational approaches. Network pharmacology is one such method that integrates bioinformatics, pharmacology, and systems biology to study drug-target-pathway interactions holistically.[21,22] Unlike traditional pharmacology, which focuses on single targets, network pharmacology considers the multidimensional effects of bioactive compounds across multiple signaling pathways. This is particularly relevant for diseases like breast cancer, where the pathogenesis involves a complex interplay of genetic, epigenetic, and environmental factors.[23] The approach enables researchers to predict therapeutic targets, identify synergistic compound interactions, and prioritize candidates for downstream validation. Moreover, it facilitates the rational design of combination therapies that can modulate several key nodes in oncogenic networks.[24] Combined with other in silico techniques such as molecular docking and dynamics simulation, network pharmacology can provide valuable insights into the pharmacodynamic profiles of natural products. Such integrative methodologies reduce the reliance on labor-intensive experimental trials, thereby accelerating drug discovery.

Given the urgent need for safer alternatives in breast cancer therapy and the therapeutic promise of plant-based compounds, *Citrus aurantium* represents a compelling candidate for further investigation. Its bioactive metabolites may act on crucial signaling pathways involved in tumor progression, hormone regulation, and immune modulation. A deeper understanding of its molecular interactions with cancer-associated proteins could inform the development of novel phytotherapeutic agents. By leveraging computational tools, researchers can map compound–target interactions and predict the structural compatibility of plant-derived ligands with relevant receptors. This approach offers a cost-effective and scientifically robust avenue for identifying new candidates for breast cancer treatment. In light of these considerations, *Citrus aurantium's* therapeutic relevance in oncology warrants further exploration, especially through network-based and molecular modeling techniques. Such investigations not only enhance our understanding of this medicinal plant but also contribute to the global effort of identifying effective and accessible therapies for breast cancer. As research progresses, *Citrus aurantium* may emerge as a valuable resource in the evolving landscape of cancer drug discovery.

2. Materials and methods

2.1. Software and database

Several computational tools and databases were employed in this study. The secondary metabolites of *Citrus aurantium* were retrieved from the KNApSAcK Family database (www.knapsackfamily.com/).[25] Canonical SMILES of each compound were used in SwissADME (www.swissadme.ch/)[26] and ProTox 3.0 (tox.charite.de/protox3/#),[27] to predict pharmacokinetics and toxicity profiles. GeneCards (genecards.org/)[28] and SwissTargetPrediction (www.swisstargetprediction.ch/) were used to gather breast cancer-related targets and compound target predictions.[29] FunRich v3.1.3 software was used to generate a Venn diagram and identify overlapping targets. STRING (string-db.org/),[30] was used to generate protein–protein interaction networks, and Cytoscape v3.10.3 with CytoHubba was used for network visualization and hub gene selection.[31] Molecular docking was performed using AutoDock Tools 1.5.7[32] and AutoDock Vina,[33] and visualized using BIOVIA Discovery Studio 2021.[34] The 3D structures of the compounds were obtained from PubChem (pubchem.ncbi.nlm.nih.gov),[35] and the protein target ESR1 (PDB ID: 1XPC) was retrieved from the Protein Data Bank (www.rcsb.org/).[36] Molecular dynamics simulations were conducted using GROMACS 2016.3[37] with ligand topology prepared via ACPYPE.[38] MM/PBSA calculations were carried out using the g_mmpbsa tool integrated into GROMACS workflows.[39]

2.2. Secondary metabolites of Citrus aurantium

The secondary metabolites of *Citrus aurantium* were obtained from the KNApSAcK Family database. This resource lists known phytochemical compounds derived from medicinal plants. All identified compounds were compiled into an Excel spreadsheet. For each compound, the corresponding canonical SMILES was extracted for use in downstream analyses. These SMILES notations served as input for pharmacokinetic and target prediction tools. Only those compounds with complete structural data were retained for further evaluation. The selection process aimed to identify diverse scaffolds with potential biological activity. The data set was also curated to remove redundant or structurally similar entries. This initial step provided a comprehensive library of bioactive compounds from *Citrus aurantium*. These compounds were then carried forward for ADME screening and molecular docking simulations.

2.3. Pharmacokinetics, drug-likeness, and toxicity analysis

The pharmacokinetic profiles of each compound were evaluated using SwissADME. Canonical SMILES were submitted individually to assess parameters like Lipinski's Rule of Five and bioavailability scores.

The analysis also included gastrointestinal absorption, water solubility, and synthetic accessibility. Compounds that violated more than one Lipinski criterion were excluded from further study. Next, ProTox 3.0 was used to predict oral toxicity, LD_{50} values, and toxicity classes. Toxicity mechanisms and structural alerts were also recorded when available. Compounds were categorized into classes 1 through 6 based on GHS toxicity criteria. All results were tabulated to compare safety profiles. This dual screening helped prioritize compounds that combined favorable pharmacokinetics with low predicted toxicity. The selected candidates were subjected to target prediction and docking analysis.

2.4. Target prediction and overlap identification

To predict protein targets relevant to breast cancer, two databases were utilized. First, GeneCards was queried using the keyword "breast cancer" to retrieve disease-related targets. Second, the SMILES of each compound were input into SwissTargetPrediction to identify compound-specific targets. Only *Homo sapiens* entries with probability scores greater than zero were retained. The resulting gene lists were compared to find overlapping targets. This intersection was visualized using a Venn diagram generated with FunRich v3.1.3. The overlapping targets were considered core targets for subsequent analysis. All identified genes were validated for relevance using STRING database annotations. These core targets were then subjected to network analysis. This approach ensured the selection of biologically meaningful interactions between compounds and disease.

2.5. Protein–protein interaction (PPI) network construction

The overlapping protein targets were uploaded into the STRING database (*Homo sapiens* organism) to construct the protein–protein interaction network. The interaction confidence score was set to high confidence (0.7) rather than the medium default (0.4), to ensure reliability of the predicted associations. The resulting network was exported in CSV format and imported into Cytoscape v3.10.3 for visualization and topological analysis. The CytoHubba plugin was used to rank and identify the top 10 hub genes based on degree centrality, representing the most highly connected and biologically influential nodes. Functional enrichment analysis was subsequently performed using STRING annotations, with an FDR-adjusted p-value ≤ 0.05 as the significance threshold. Only Gene Ontology (GO) and KEGG categories were retained, and redundant terms were filtered using a similarity cutoff of 0.5. The top enriched pathways and biological processes were summarized with adjusted p-values and gene counts. This network-based analysis provided a robust systems-level understanding of how *Citrus aurantium* metabolites potentially modulate cancer-related molecular interactions.

2.6. Molecular docking

Molecular docking was performed using AutoDock Tools 1.5.7 and AutoDock Vina to predict the binding interactions between selected *Citrus aurantium* compounds and ESR1 (PDB ID: 1XPC), which was chosen due to its high connectivity in the PPI network. The protein structure was prepared by removing crystallographic water molecules, separating native ligands, adding polar hydrogens, and assigning Kollman charges using BIOVIA Discovery Studio 2021. Missing residues in the crystal structure were repaired using the Molecular Operating Environment (MOE) software. Ligand structures were retrieved from PubChem in SDF format and converted into PDB using BIOVIA Discovery Studio, then further converted into PDBQT format in AutoDock Tools. The docking grid was set to encompass the ESR1 active site with dimensions of $64 \times 60 \times 60$ points (x, y, z), a grid spacing of 0.375 Å, and a grid center at (30.751, −1.346, 23.816). The docking parameters included an exhaustiveness corresponding to 100 genetic algorithm runs (ga_run = 100) and standard local search and GA-LS hybrid optimization parameters: ga_pop_size = 150, ga_num_evals = 250000, ga_num_generations = 27000, ga_mutation_rate = 0.02, and ga_crossover_rate = 0.8. Clustering was performed using an RMS tolerance of 2.0 Å with ranked cluster analysis. The redocking validation of the native ligand yielded an RMSD of 0.52 Å, confirming the reliability of the docking protocol. Known ESR1 modulators such as benzoxathiin-based SERMs were included as positive controls, while a decoy ligand set was used to estimate the false-positive rate. Binding affinities were recorded in kcal/mol, and docking poses were visualized in BIOVIA Discovery Studio 2021.

2.7. Molecular dynamics simulation

The best ligand–receptor complex obtained from molecular docking was subjected to molecular dynamics (MD) simulation using GROMACS 2016.3. The AMBER99SB-ILDN force field was applied for the protein, while ligand topologies were generated using ACPYPE based on the General AMBER Force Field (GAFF) with AM1-BCC charge model. The complex was solvated in a triclinic box with a minimum distance of 1.0 nm between the protein surface and the box edge, using the SPC/E water model. Counterions (Na^+ and Cl^-) were added to neutralize the system and maintain physiological ionic strength. Energy minimization was performed using the steepest descent algorithm for 5000 steps until the maximum force converged below 1000 kJ/mol·nm. The equilibrations were conducted in two phases: NVT (constant number of particles, volume, and temperature) for 1 ns and NPT (constant number of particles, pressure, and temperature) for another 1 ns, both maintained at 300 K using the V-rescale thermostat and 1 bar using the Parrinello–Rahman barostat. All covalent bonds involving hydrogen atoms were constrained using the LINCS algorithm. Long-range electrostatic interactions were treated with the Particle Mesh Ewald (PME) method, and a cutoff distance of 1.0 nm was applied for both Coulombic and van der Waals interactions. A time step of 2 fs was used, and coordinates were saved every 100 ps for analysis. A 300 ns production run was performed to evaluate the conformational stability and dynamic behavior of the complex. The SPC/E water model was selected for compatibility testing with AMBER99SB-ILDN, and its suitability was confirmed through prior benchmarks showing consistent hydrogen-bonding and dielectric properties. Post-simulation analyses included root mean square deviation (RMSD), root mean square fluctuation (RMSF), radius of gyration (Rg), solvent-accessible surface area (SASA), and hydrogen bond occupancy, which collectively assessed the complex's stability, compactness, and intermolecular interaction persistence throughout the simulation.

2.8. MM/PBSA free energy calculation

Binding free energy calculations were performed using the MM/PBSA method. The g_mmpbsa tool was used to analyze 30 snapshots from the 300 ns MD simulation. Energy terms included van der Waals, electrostatic, polar solvation, and non-polar solvation contributions. Each component was averaged across all frames. The total binding free energy provided quantitative insight into ligand affinity. Residue decomposition analysis was also conducted to identify key contributors to binding. The results were reported in kJ/mol. Compounds with the lowest binding free energy were considered to have the strongest interactions. This method validated docking results with more dynamic energy profiles. The MM/PBSA values complemented structural observations from MD simulation.

3. Results

3.1. Pharmacokinetics and toxicity of Citrus aurantium compounds

Pharmacokinetic evaluation of 111 metabolites derived from *Citrus aurantium* revealed full compliance with Lipinski's Rule of Five,

indicating favorable oral drug-likeness. Most compounds exhibited a bioavailability score of 0.55, suggesting moderate to good absorption potential *in vivo*. Several metabolites, such as 3,4-dimethoxybenzoic acid and 4-Methoxybenzoic acid, stood out with higher scores of 0.85, enhancing their potential as drug candidates.[40] The physicochemical characteristics, including molecular weight, hydrogen bond acceptors, and lipophilicity, fell within acceptable ranges for all compounds. The majority of the metabolites were classified under toxicity class 5 based on LD_{50} values, which implies low acute toxicity.[41] Terpenoids like espatulenol, limonene, and nobiletin showed high LD_{50} values above 3000 mg/kg, supporting their safety. Some metabolites including indole, quinoline, and malonaldehyde were categorized as class 4, with LD_{50} values ranging from 331 to 606 mg/kg, indicating moderate toxicity. A few compounds such as neohesperidin, teresantanane, and linalyl acetate reached class 6 with LD_{50} values up to 12,000 mg/kg, highlighting their excellent safety profile. These results reflect structural diversity among compounds, contributing to variability in toxicity levels. The summary of pharmacokinetic and toxicity characteristics for all compounds is provided in Table 1.

The analysis of chemical subclasses revealed consistent trends in both pharmacokinetics and toxicity outcomes. Flavonoids like hesperetin, diosmetin, and naringenin derivatives were mostly in toxicity class 4, with LD_{50} values around 2000 mg/kg. Polymethoxylated flavones such as nobiletin and tangeretin demonstrated superior safety, consistently classified in class 5 or higher. Monoterpene alcohols like geraniol and citronellol showed LD_{50} values above 4000 mg/kg, maintaining class 5 classification. Aldehyde derivatives including octanal and nonadienal showed slightly lower LD_{50} values, yet remained within the threshold for class 5. Borderline compounds such as methyl anthranilate and isopropyl alcohol hovered near class 4 cutoffs, warranting closer evaluation. Sesquiterpenes including beta-caryophyllene and alpha-farnesene exhibited high LD_{50} values and acceptable drug-likeness, suggesting their potential use. Synephrine and epoxybergamottin, key bioactives in *Citrus aurantium*, showed both favorable ADME profiles and low toxicity. Generally, the metabolite composition reflects a balance between efficacy and safety that is desirable in candidate compounds. The data supports the advancement of several compounds for further docking and simulation analysis. These profiles confirm that *Citrus aurantium* harbors a wide range of bioactive compounds with promising pharmacological properties.

3.2. Identification of overlapping targets between Citrus aurantium metabolites and breast cancer

To identify potential therapeutic targets, intersecting genes between *Citrus aurantium* metabolites and breast cancer were determined using a Venn diagram approach. The total number of predicted targets from *Citrus aurantium* metabolites was 683, while 218 breast cancer-related targets were obtained from GeneCards and DisGeNET databases. Through comparative analysis, 39 genes were found to be common between these two datasets. These overlapping genes represent potential molecular links through which the phytochemicals may exert anticancer effects. The remaining 644 genes were unique to *Citrus aurantium* metabolites, while 179 were specific to breast cancer. The presence of overlapping targets implies potential modulation of cancer-related biological pathways. These 39 common genes serve as candidate targets for downstream molecular docking and enrichment analysis. The use of intersecting target analysis is fundamental in network pharmacology as it narrows down the biological relevance of compounds. This overlap is visually summarized in the Venn diagram presented in Fig. 1. The integration of disease and compound targets provides a focused framework for elucidating bioactive mechanisms.

The identification of these 39 intersecting targets highlights the multi-target nature of *Citrus aurantium* metabolites. Such multi-target potential is aligned with the pharmacological complexity of herbal medicine. Some of the shared targets are known to play central roles in cancer progression, including genes related to proliferation, apoptosis, and angiogenesis.[42] By focusing on this intersection, researchers can prioritize genes for molecular docking and validation experiments. Moreover, network visualization and PPI analysis of these targets can further reveal key hubs in breast cancer modulation. The absence of significant overlap would have limited the mechanistic interpretation of bioactivity. However, the existence of 39 shared targets justifies continued in silico and experimental exploration. These genes form the basis for enrichment analysis in GO and KEGG databases. Their functional roles can be studied in the context of cellular localization, binding activity, and pathway regulation. This strategy enhances the rational selection of candidate molecules with potential anti-breast cancer activity.

3.3. Construction and analysis of PPI network of overlapping targets

The protein–protein interaction (PPI) network analysis was conducted to explore the interconnectivity among the 39 overlapping targets of *Citrus aurantium* and breast cancer. Using the STRING database with a high-confidence interaction threshold (combined score ≥ 0.7), we generated a PPI network that was subsequently visualized and analyzed in Cytoscape. Network topology was evaluated (degree and betweenness centrality, clustering coefficient) to prioritize putative hub nodes and information-flow bottlenecks. To contextualize network biology, functional enrichment was performed for Gene Ontology (biological process, molecular function, cellular component) and KEGG pathways with FDR-adjusted p-value ≤ 0.05; redundant terms were minimized using a similarity cutoff of 0.5, and the top non-redundant terms are reported with adjusted p-values and gene counts. The network provides insight into how these proteins functionally interact to mediate biological processes relevant to cancer. As depicted in Fig. 2, most of the proteins form a highly interconnected network with a few peripheral nodes. Central hubs in the network such as ESR1, AKT1, BCL2, and CCND1 showed higher connectivity, indicating their critical roles in signaling cascades. The dense interactions suggest that these targets may participate in coordinated pathways governing cell cycle regulation, apoptosis, and hormonal signaling. The network highlights the multi-target potential of *Citrus aurantium* constituents in modulating complex biological responses. Notably, several of the proteins identified are known oncogenes or tumor suppressors in breast cancer. This comprehensive network representation enhances the understanding of molecular mechanisms involved in therapeutic effects.

A closer examination of the interaction map reveals functional modules and key regulatory nodes within the system. The presence of transcription factors such as ESR1 and AR suggests hormonal pathway involvement. Anti-apoptotic proteins like BCL2 and MCL1 reinforce the relevance of this network in cancer cell survival.[43] The inclusion of CDKs (e.g., CDK2, CDK6) and cyclins (e.g., CCND1) points to the modulation of cell cycle checkpoints.[44] Other notable nodes include PI3K/AKT signaling elements, such as PIK3CA and AKT1, known to regulate proliferation and metabolic activity.[45] The functional diversity of the proteins involved indicates that the anti-breast cancer potential of *Citrus aurantium* is not limited to a single pathway. Instead, it reflects a systems pharmacology approach targeting multiple biological layers. The PPI network also provides the foundation for subsequent centrality and topology analysis. Hub genes identified through degree value and betweenness metrics will guide further docking and validation studies. Altogether, the PPI network validates the therapeutic plausibility of the 39 shared targets and uncovers potential molecular mechanisms for *Citrus aurantium's* anticancer activity.

3.4. Identification and visualization of hub genes in the PPI network

To further refine the PPI network analysis, a hub gene identification step was performed to highlight the most central and influential targets. This was done using network topology parameters such as degree

Table 1
Pharmacokinetic and toxicity profiles of *Citrus aurantium* metabolites.

No	Compound ID	Metabolite	Molecular Weight	Molar refractivity	TPSA	Consensus Log $P_{o/w}$	Log S (ESOL)	Lipinski	Bioavailability Score	Synthetic Accessibility	LD_{50}	Toxicity Class
1	C00000149	Espatulenol	220.35 g/mol	68.34	20.23 Å^2	3.30	−3.17	Yes	0.55	3.78	3900 mg/kg	5
2	C00000153	cis-p-Menth-2-en-1-ol	154.25 g/mol	48.80	20.23 Å^2	2.29	−2.17	Yes	0.55	3.51	2340 mg/kg	5
3	C00000154	trans-p-Menth-2-en-1-ol	154.25 g/mol	48.80	20.23 Å^2	2.30	−2.17	Yes	0.55	3.51	2340 mg/kg	5
4	C00000184	alpha-Thujene	136.23 g/mol	45.22	0.00 Å^2	3.15	−2.41	Yes	0.55	3.99	5000 mg/kg	5
5	C00000300	Seselin	228.24 g/mol	66.61	39.44 Å^2	2.81	−3.47	Yes	0.55	3.39	3850 mg/kg	5
6	C00000357	Hexanal	100.16 g/mol	31.16	17.07 Å^2	1.66	−1.32	Yes	0.55	1.06	3240 mg/kg	5
7	C00000674	5,7,3′,4′-Tetrahydroxyflavone	286.24 g/mol	76.01	111.13 Å^2	1.73	−3.71	Yes	0.55	3.02	3919 mg/kg	5
8	C00000805	alpha-Pinene	136.23 g/mol	45.22	0.00 Å^2	3.44	−3.51	Yes	0.55	4.44	3700 mg/kg	5
9	C00000816	beta-Pinene	136.23 g/mol	45.22	0.00 Å^2	3.42	−3.31	Yes	0.55	3.73	4700 mg/kg	5
10	C00000823	Limonene	136.23 g/mol	47.12	0.00 Å^2	3.37	−3.50	Yes	0.55	3.46	4400 mg/kg	5
11	C00000830	cis-Sabinene hydrate	154.25 g/mol	46.90	20.23 Å^2	2.31	−2.07	Yes	0.55	2.82	2000 mg/kg	4
12	C00000839	3-Carene	136.23 g/mol	45.22	0.00 Å^2	3.42	−3.44	Yes	0.55	3.84	4800 mg/kg	5
13	C00000844	Citronellol	156.27 g/mol	50.87	20.23 Å^2	2.92	−2.94	Yes	0.55	2.61	3450 mg/kg	5
14	C00000845	(E)-geraniol	154.25 g/mol	50.40	20.23 Å^2	2.74	−2.78	Yes	0.55	2.58	2100 mg/kg	5
15	C00000853	beta-Myrcene	136.23 g/mol	48.76	0.00 Å^2	3.43	−3.05	Yes	0.55	2.85	5000 mg/kg	5
16	C00000855	beta-Nerol	154.25 g/mol	50.40	20.23 Å^2	2.78	−2.78	Yes	0.55	2.58	2100 mg/kg	5
17	C00000861	alpha-Terpinolene	136.23 g/mol	47.12	0.00 Å^2	3.40	−3.50	Yes	0.55	2.98	4390 mg/kg	5
18	C00000960	Eriodictyol	288.25 g/mol	73.59	107.22 Å^2	1.45	−3.26	Yes	0.55	3.11	2000 mg/kg	4
19	C00000968	Hesperetin	302.28 g/mol	78.06	96.22 Å^2	1.91	−3.62	Yes	0.55	3.22	2000 mg/kg	4
20	C00000987	Neohesperidin	610.56 g/mol	141.41	234.29 Å^2	−0.77	−3.07	Yes	0.55	6.36	12000 mg/kg	6
21	C00000995	Poncirin	610.56 g/mol	141.41	234.29 Å^2	−0.77	−3.07	Yes	0.55	6.36	2300 mg/kg	5
22	C00000998	Naringenin 7-O-beta-D-glucoside	434.39 g/mol	103.69	166.14 Å^2	0.16	−2.97	Yes	0.55	4.98	2300 mg/kg	5
23	C00001036	Diosmetin	300.26 g/mol	80.48	100.13 Å^2	2.19	−4.06	Yes	0.55	3.05	3919 mg/kg	5
24	C00001076	Nobiletin	402.39 g/mol	106.87	85.59 Å^2	3.02	−4.18	Yes	0.55	3.90	5000 mg/kg	5
25	C00001105	Tangeretin	372.37 g/mol	100.38	76.36 Å^2	3.02	−4.11	Yes	0.55	3.74	5000 mg/kg	5
26	C00001313	(Z)-Jasmone	164.24 g/mol	52.13	17.07 Å^2	2.74	−2.05	Yes	0.55	2.98	5000 mg/kg	5
27	C00001417	Hordenine	165.23 g/mol	50.75	23.47 Å^2	1.82	−2.35	Yes	0.55	1.00	2859 mg/kg	5
28	C00001418	Indole	117.15 g/mol	38.30	15.79 Å^2	1.98	−2.60	Yes	0.55	1.00	360 mg/kg	4
29	C00001425	Octopamine	153.18 g/mol	42.11	66.48 Å^2	0.20	−0.49	Yes	0.55	1.35	1090 mg/kg	4
30	C00001435	Tyramine	137.18 g/mol	40.95	46.25 Å^2	1.17	−1.70	Yes	0.55	1.00	1091 mg/kg	4
31	C00002663	2-Phenylethanol	122.16 g/mol	37.38	20.23 Å^2	1.64	−1.82	Yes	0.55	1.00	800 mg/kg	4
32	C00002780	Feruloylputrescine	264.32 g/mol	74.79	84.58 Å^2	1.45	−1.83	Yes	0.55	2.40	1180 mg/kg	4
33	C00003029	Camphene	136.23 g/mol	45.22	0.00 Å^2	3.43	−3.34	Yes	0.55	3.50	5000 mg/kg	5
34	C00003035	trans-Citral	152.23 g/mol	49.44	17.07 Å^2	2.71	−2.43	Yes	0.55	2.49	500 mg/kg	4
35	C00003036	cis-Citral	152.23 g/mol	49.44	17.07 Å^2	2.71	−2.43	Yes	0.55	2.49	500 mg/kg	4
36	C00003043	Dipentene	136.23 g/mol	47.12	0.00 Å^2	3.37	−3.50	Yes	0.55	3.46	4400 mg/kg	5
37	C00003046	Geranyl acetate	196.29 g/mol	60.13	26.30 Å^2	3.21	−3.21	Yes	0.55	2.72	5000 mg/kg	5
38	C00003047	(+-)-Linalool	154.25 g/mol	50.44	20.23 Å^2	2.66	−2.40	Yes	0.55	2.74	2200 mg/kg	5
39	C00003048	Linalyl acetate	196.29 g/mol	60.17	26.30 Å^2	3.24	−3.14	Yes	0.55	2.75	12000 mg/kg	6
40	C00003051	alpha-Phellandrene	136.23 g/mol	47.12	0.00 Å^2	2.97	−2.64	Yes	0.55	4.15	5700 mg/kg	6
41	C00003060	alpha-Terpinene	136.23 g/mol	47.12	0.00 Å^2	3.30	−3.30	Yes	0.55	3.63	1680 mg/kg	4
42	C00003061	gamma-Terpinene	136.23 g/mol	47.12	0.00 Å^2	3.35	−3.45	Yes	0.55	3.11	5300 mg/kg	5
43	C00003110	beta-Caryophyllene	204.35 g/mol	68.78	0.00 Å^2	4.24	−3.87	Yes	0.55	4.51	5300 mg/kg	5
44	C00003118	alpha-Copaene	204.35 g/mol	67.14	0.00 Å^2	4.30	−3.86	Yes	0.55	4.62	3700 mg/kg	5
45	C00003130	alpha-Farnesene	204.35 g/mol	72.32	0.00 Å^2	4.96	−4.57	Yes	0.55	3.72	3650 mg/kg	5
46	C00003131	E-beta-farnesene	204.35 g/mol	72.32	0.00 Å^2	4.97	−4.44	Yes	0.55	3.42	5000 mg/kg	5
47	C00003147	alpha-Caryophyllene (obsol.)	204.35 g/mol	70.42	0.00 Å^2	4.26	−3.97	Yes	0.55	3.66	3650 mg/kg	5
48	C00003166	Nerolidol	222.37 g/mol	74.00	20.23 Å^2	4.19	−3.80	Yes	0.55	3.53	5000 mg/kg	5
49	C00003467	Phytol	296.53 g/mol	98.94	20.23 Å^2	6.23	−5.98	Yes	0.55	4.30	5000 mg/kg	5
50	C00003817	Apigenin	270.24 g/mol	73.99	90.90 Å^2	2.11	−3.94	Yes	0.55	2.96	2500 mg/kg	5
51	C00003821	5,7,4′-Trimethoxyflavone	312.32 g/mol	87.40	57.90 Å^2	3.10	−4.20	Yes	0.55	3.28	3919 mg/kg	5
52	C00003841	Scutellarein 5,6,7,4′-tetramethyl ether	342.34 g/mol	93.89	67.13 Å^2	3.01	−4.04	Yes	0.55	3.51	4000 mg/kg	5
53	C00003912	Isosinensetin	372.37 g/mol	100.38	76.36 Å^2	2.98	−4.11	Yes	0.55	3.71	5000 mg/kg	5

(*continued on next page*)

Table 1 (*continued*)

No	Compound ID	Metabolite	Molecular Weight	Molar refractivity	TPSA	Consensus Log $P_{o/w}$	Log S (ESOL)	Lipinski	Bioavailability Score	Synthetic Accessibility	LD_{50}	Toxicity Class
54	C00003936	5-Demethylnobiletin	388.37 g/mol	102.40	96.59 Å^2	2.78	−4.31	Yes	0.55	3.76	5000 mg/kg	5
55	C00004657	Auranetin	372.37 g/mol	100.38	76.36 Å^2	3.08	−4.24	Yes	0.55	3.74	5000 mg/kg	5
56	C00004673	5-Hydroxyauranetin	388.37 g/mol	102.40	96.59 Å^2	2.86	−4.44	Yes	0.55	3.78	5000 mg/kg	5
57	C00007242	beta-Bisabolene	204.35 g/mol	70.68	0.00 Å^2	4.83	−4.89	Yes	0.55	3.90	4400 mg/kg	5
58	C00007453	beta-Elemene	204.35 g/mol	70.42	0.00 Å^2	4.65	−4.76	Yes	0.55	3.63	5000 mg/kg	5
59	C00007636	delta-Cadinene	204.35 g/mol	69.04	0.00 Å^2	4.14	−3.43	Yes	0.55	4.14	4390 mg/kg	5
60	C00010301	(+)-S-Linalool	154.25 g/mol	50.44	20.23 Å^2	2.66	−2.40	Yes	0.55	2.74	2200 mg/kg	5
61	C00010325	Epoxylinalool	170.25 g/mol	49.92	29.46 Å^2	2.05	−2.29	Yes	0.55	3.20	2500 mg/kg	5
62	C00010872	beta-Phellandrene	136.23 g/mol	47.12	0.00 Å^2	3.07	−2.79	Yes	0.55	3.73	5000 mg/kg	5
63	C00010875	2,4(8)-p-Menthadiene	136.23 g/mol	46.12	0.00 Å^2	3.09	−2.90	Yes	0.55	3.72	7000 mg/kg	6
64	C00010905	4-Isopropenyl-1-methylbenzene	132,20 g/mol	46.31	0.00 Å^2	3.37	−3.36	Yes	0.55	1.21	2255 mg/kg	4
65	C00010974	alpha-Cymene	134.22 g/mol	45.99	0.00 Å^2	3.54	−3.81	Yes	0.55	1.00	1370 mg/kg	4
66	C00011067	Teresantanane	136.23 g/mol	43.32	0.00 Å^2	3.14	−2.73	Yes	0.55	3.59	15380 mg/kg	6
67	C00012011	delta-Elemene	204.35 g/mol	70.42	0.00 Å^2	4.49	−4.23	Yes	0.55	4.25	5300 mg/kg	5
68	C00012425	(+)-Bicyclogermacrene	204.35 g/mol	68.78	0.00 Å^2	4.12	−3.72	Yes	0.55	4.34	5300 mg/kg	5
69	C00013304	4′,5,7,8-Tetramethoxyflavone	342.34 g/mol	93.89	67.13 Å^2	3.00	−4.04	Yes	0.55	3.55	4000 mg/kg	5
70	C00013596	Sinensetin	372.37 g/mol	100.38	76.36 Å^2	3.10	−4.40	Yes	0.55	3.68	5000 mg/kg	5
71	C00019560	Ethanol	46.07 g/mol	12.89	20.23 Å^2	0.09	−0.07	Yes	0.55	1.00	3450 mg/kg	5
72	C00021903	trans-alpha-Bergamotene	204.35 g/mol	68.78	0.00 Å^2	4.73	−4.97	Yes	0.55	5.07	3700 mg/kg	5
73	C00026478	Quinoline	129.16 g/mol	41.74	12.89 Å^2	2.08	−2.66	Yes	0.55	1.00	331 mg/kg	4
74	C00027432	N-Methyltyramine	151.21 g/mol	45.85	32.26 Å^2	1.57	−2.00	Yes	0.55	1.00	2859 mg/kg	5
75	C00029335	(E)-beta-Ocimene	136.23 g/mol	48.76	0.00 Å^2	3.40	−3.17	Yes	0.55	3.63	113 mg/kg	5
76	C00029339	(6E)-3,7,11-Trimethyl-1,6,10-dodecatrien-3-ol	222.37 g/mol	74.00	20.23 Å^2	4.19	−3.80	Yes	0.55	3.53	5000 mg/kg	5
77	C00029350	cis-beta-Farnesene	204.35 g/mol	72.32	0.00 Å^2	4.97	−4.44	Yes	0.55	3.42	5000 mg/kg	5
78	C00029479	3,4-dimethoxybenzoic acid	182.17 g/mol	46.39	55.76 Å^2	1.39	−2.13	Yes	0.85	1.55	2000 mg/kg	4
79	C00029536	4-Methoxybenzoic acid	152.15 g/mol	39.89	46.53 Å^2	1.49	−2.29	Yes	0.85	1.00	2200 mg/kg	5
80	C00029544	4-Terpineol	154.25 g/mol	48.80	20.23 Å^2	2.60	−2.78	Yes	0.55	3.28	1016 mg/kg	4
81	C00029674	alpha-Terpineol	154.25 g/mol	48.80	20.23 Å^2	2.58	−2.87	Yes	0.55	3.24	2830 mg/kg	5
82	C00029763	Aurapten	298.38 g/mol	91.29	39.44 Å^2	4.51	−4.84	Yes	0.55	3.43	3200 mg/kg	5
83	C00030099	Decanal	156.27 g/mol	50.38	17.07 Å^2	3.17	−2.67	Yes	0.55	1.62	5000 mg/kg	5
84	C00030828	Nonadienal	138.21 g/mol	44.63	17.07 Å^2	2.45	−2.07	Yes	0.55	2.87	5000 mg/kg	5
85	C00030880	Octanal	128.21 g/mol	40.77	17.07 Å^2	2.42	−1.95	Yes	0.55	1.43	5000 mg/kg	5
86	C00031258	4(10)-Thujene	136.23 g/mol	45.22	0.00 Å^2	3.25	−2.57	Yes	0.55	2.87	5000 mg/kg	5
87	C00034600	Methyl anthranilate	151.16 g/mol	42.13	52.32 Å^2	1.40	−2.23	Yes	0.55	1.00	2910 mg/kg	5
88	C00034775	6-Methyl-5-hepten-2-one	126.20 g/mol	40.30	17.07 Å^2	2.07	−1.61	Yes	0.55	2.22	2400 mg/kg	5
89	C00034989	(E)-Ocimene	136.23 g/mol	48.76	0.00 Å^2	3.40	−3.17	Yes	0.55	3.63	7000 mg/kg	6
90	C00035043	alpha-terpineol acetate	196.29 g/mol	58.53	26.3 Å^2	3.04	−3.35	Yes	0.55	3.13	4800 mg/kg	5
91	C00035130	Methyl geranate	182.26 g/mol	55.33	26.30 Å^2	2.91	−2.79	Yes	0.55	2.65	5000 mg/kg	5
92	C00035138	Neryl acetate	196.29 g/mol	60.13	26.30 Å^2	3.21	−3.21	Yes	0.55	2.72	5000 mg/kg	5
93	C00035823	Citronellal	154.25 g/mol	49.91	17.07 Å^2	2.94	−2.88	Yes	0.55	2.57	2420 mg/kg	5
94	C00036308	D-germacrene	204.35 g/mol	70.68	0.00 Å^2	4.57	−4.74	Yes	0.55	4.10	4400 mg/kg	5
95	C00046607	alpha-Curcumene	202.34 g/mol	69.55	0.00 Å^2	4.86	−4.52	Yes	0.55	2.31	2000 mg/kg	4
96	C00048263	2,6-Dimethyl-1,3,5,7-octatetraene	134.22 g/mol	48.29	0.00 Å^2	3.35	−3.23	Yes	0.55	3.93	1900 mg/kg	4
97	C00048304	Acetone	58.08 g/mol	16.73	17.07 Å^2	0.40	−0.17	Yes	0.55	1.00	3000 mg/kg	5
98	C00048310	2,6-Dimethyl-2,4,6-octatriene	136.23 g/mol	48.76	0.00 Å^2	3.37	−3.20	Yes	0.55	4.00	1900 mg/kg	4
99	C00048315	alpha-Myrcene	136.23 g/mol	48.76	0.00 Å^2	3.55	−3.28	Yes	0.55	2.32	5050 mg/kg	6
100	C00048350	Carvyl acetate	194.27 g/mol	58.02	26.30 Å^2	2.84	−3.17	Yes	0.55	3.63	5000 mg/kg	5
101	C00048438	Isopropyl alcohol	60.10 g/mol	17.70	20.23 Å^2	0.45	−0.43	Yes	0.55	1.00	2733 mg/kg	4
102	C00048486	Neo-allo-ocimene	136.23 g/mol	48.76	0.00 Å^2	3.37	−3.20	Yes	0.55	4.00	1900 mg/kg	4
103	C00048498	n-Phenylformamide	121.14 g/mol	36.34	29.10 Å^2	1.27	−1.65	Yes	0.55	1.00	800 mg/kg	4
104	C00051735	Synephrine	167.21 g/mol	47.01	52.49 Å^2	0.55	−0.66	Yes	0.55	1.48	4450 mg/kg	5
105	C00053039	Epoxybergamottin	354.40 g/mol	100.55	65.11 Å^2	4.15	−4.52	Yes	0.55	4.18	4000 mg/kg	5
106	C00053122	cis-ocimene	138.25 g/mol	49.24	0.00 Å^2	3.53	−3.25	Yes	0.55	3.08	7000 mg/kg	6
107	C00053828	Tetrahydrolinalool	158.28 g/mol	51.38	20.23 Å^2	2.90	−2.55	Yes	0.55	2.10	1000 mg/kg	4

(*continued on next page*)

Table 1 (*continued*)

No	Compound ID	Metabolite	Molecular Weight	Molar refractivity	TPSA	Consensus Log $P_{o/w}$	Log S (ESOL)	Lipinski	Bioavailability Score	Synthetic Accessibility	LD_{50}	Toxicity Class
108	C00053869	1-Tritriacontanol	480.89 g/mol	161.91	20.23 Å^2	11.59	−11.06	Yes	0.55	4.35	1000 mg/kg	4
109	C00056187	trans-Carvyl acetate	194.27 g/mol	58.02	26.30 Å^2	2.83	−3.17	Yes	0.55	3.63	5000 mg/kg	5
110	C00059951	Linalyl propionate	210.31 g/mol	64.98	26.30 Å^2	3.61	−3.45	Yes	0.55	2.96	5000 mg/kg	5
111	C00062142	Malonaldehyde	72.06 g/mol	16.93	34.14 Å^2	−0.24	0.25	Yes	0.55	1.00	606 mg/kg	4

No	Compound ID	Metabolite	GI Absorption	BBB Permeant	P-gp Substrate	CYP1A2 Inhibitor	CYP2C19 Inhibitor	CYP2C9 Inhibitor	CYP2D6 Inhibitor	CYP3A4 Inhibitor
1	C00000149	Espatulenol	High	Yes	No	No	Yes	No	No	No
2	C00000153	cis-p-Menth-2-en-1-ol	High	Yes	No	No	No	No	No	No
3	C00000154	trans-p-Menth-2-en-1-ol	High	Yes	No	No	No	No	No	No
4	C00000184	alpha-Thujene	Low	Yes	No	No	No	No	No	No
5	C00000300	Seselin	High	Yes	No	Yes	Yes	No	No	No
6	C00000357	Hexanal	High	Yes	No	No	No	No	No	No
7	C00000674	5,7,3′,4′-Tetrahydroxyflavone	High	No	No	Yes	No	No	Yes	Yes
8	C00000805	alpha-Pinene	Low	Yes	No	No	No	Yes	No	No
9	C00000816	beta-Pinene	Low	Yes	No	No	No	Yes	No	No
10	C00000823	Limonene	Low	Yes	No	No	No	Yes	No	No
11	C00000830	cis-Sabinene hydrate	High	Yes	No	No	No	No	No	No
12	C00000839	3-Carene	Low	Yes	No	No	No	Yes	No	No
13	C00000844	Citronellol	High	Yes	No	No	No	No	No	No
14	C00000845	(E)-geraniol	High	Yes	No	No	No	No	No	No
15	C00000853	beta-Myrcene	Low	Yes	No	No	No	No	No	No
16	C00000855	beta-Nerol	High	Yes	No	No	No	No	No	No
17	C00000861	alpha-Terpinolene	Low	Yes	No	No	No	Yes	No	No
18	C00000960	Eriodictyol	High	No	Yes	No	No	No	No	Yes
19	C00000968	Hesperetin	High	No	Yes	Yes	No	No	No	Yes
20	C00000987	Neohesperidin	Low	No	Yes	No	No	No	No	No
21	C00000995	Poncirin	Low	No	Yes	No	No	No	No	No
22	C00000998	Naringenin 7-O-beta-D-glucoside	Low	No	Yes	No	No	No	No	No
23	C00001036	Diosmetin	High	No	No	Yes	No	Yes	Yes	Yes
24	C00001076	Nobiletin	High	No	No	No	No	Yes	No	Yes
25	C00001105	Tangeretin	High	Yes	No	No	No	Yes	No	Yes
26	C00001313	(Z)-Jasmone	High	Yes	No	No	No	No	No	No
27	C00001417	Hordenine	High	Yes	No	Yes	No	No	No	No
28	C00001418	Indole	High	Yes	No	Yes	No	No	No	No
29	C00001425	Octopamine	High	No	No	No	No	No	No	No
30	C00001435	Tyramine	High	Yes	No	No	No	No	No	No
31	C00002663	2-Phenylethanol	High	Yes	No	Yes	No	No	No	No
32	C00002780	Feruloylputrescine	High	No	No	No	No	No	No	No
33	C00003029	Camphene	Low	Yes	No	No	No	Yes	No	No
34	C00003035	trans-Citral	High	Yes	No	No	No	No	No	No
35	C00003036	cis-Citral	High	Yes	No	No	No	No	No	No
36	C00003043	Dipentene	Low	Yes	No	No	No	Yes	No	No
37	C00003046	Geranyl acetate	High	Yes	No	No	No	No	No	No
38	C00003047	(+-)-Linalool	High	Yes	No	No	No	No	No	No
39	C00003048	Linalyl acetate	High	Yes	No	No	No	No	No	No
40	C00003051	alpha-Phellandrene	Low	Yes	No	No	No	No	No	No
41	C00003060	alpha-Terpinene	Low	Yes	No	No	No	No	No	No
42	C00003061	gamma-Terpinene	Low	Yes	No	No	No	No	No	No
43	C00003110	beta-Caryophyllene	Low	No	No	No	Yes	Yes	No	No
44	C00003118	alpha-Copaene	Low	Yes	No	Yes	Yes	Yes	No	No
45	C00003130	alpha-Farnesene	Low	No	No	Yes	No	Yes	No	No
46	C00003131	E-beta-farnesene	Low	No	No	Yes	No	Yes	No	No
47	C00003147	alpha-Caryophyllene (obsol.)	Low	No	No	No	No	Yes	No	No
48	C00003166	Nerolidol	High	Yes	No	Yes	No	Yes	No	No
49	C00003467	Phytol	Low	No	Yes	No	No	Yes	No	No

(*continued on next page*)

Table 1 (*continued*)

No	Compound ID	Metabolite	GI Absorption	BBB Permeant	P-gp Substrate	CYP1A2 Inhibitor	CYP2C19 Inhibitor	CYP2C9 Inhibitor	CYP2D6 Inhibitor	CYP3A4 Inhibitor
50	C00003817	Apigenin	High	No	No	Yes	No	No	Yes	Yes
51	C00003821	5,7,4′-Trimethoxyflavone	High	Yes	No	Yes	Yes	Yes	Yes	Yes
52	C00003841	Scutellarein 5,6,7,4′-tetramethyl ether	High	Yes	No	Yes	Yes	Yes	Yes	Yes
53	C00003912	Isosinensetin	High	Yes	No	No	No	Yes	No	Yes
54	C00003936	5-Demethylnobiletin	High	No	No	No	No	Yes	No	Yes
55	C00004657	Auranetin	High	Yes	No	No	No	Yes	No	Yes
56	C00004673	5-Hydroxyauranetin	High	No	No	No	No	Yes	No	Yes
57	C00007242	beta-Bisabolene	Low	No	No	No	No	Yes	No	No
58	C00007453	beta-Elemene	Low	No	No	No	Yes	Yes	No	No
59	C00007636	delta-Cadinene	Low	No	No	No	Yes	Yes	No	No
60	C00010301	(+)-S-Linalool	High	Yes	No	No	No	No	No	No
61	C00010325	Epoxylinalool	High	Yes	No	No	No	No	No	No
62	C00010872	beta-Phellandrene	Low	Yes	No	No	No	No	No	No
63	C00010875	2,4(8)-p-Menthadiene	Low	Yes	No	No	No	Yes	No	No
64	C00010905	4-Isopropenyl-1-methylbenzene	Low	Yes	No	No	No	No	Yes	No
65	C00010974	alpha-Cymene	Low	Yes	No	No	No	No	Yes	No
66	C00011067	Teresantanane	Low	Yes	No	No	No	No	No	No
67	C00012011	delta-Elemene	Low	No	No	No	Yes	Yes	No	No
68	C00012425	(+)-Bicyclogermacrene	Low	No	No	No	Yes	Yes	No	No
69	C00013304	4′,5,7,8-Tetramethoxyflavone	High	Yes	No	Yes	Yes	yes	Yes	Yes
70	C00013596	Sinensetin	High	Yes	No	No	Yes	yes	No	Yes
71	C00019560	Ethanol	Low	No	No	No	No	No	No	No
72	C00021903	trans-alpha-Bergamotene	Low	No	No	No	Yes	Yes	No	No
73	C00026478	Quinoline	High	Yes	No	Yes	No	No	No	No
74	C00027432	N-Methyltyramine	High	Yes	No	Yes	No	No	No	No
75	C00029335	(E)-beta-Ocimene	Low	Yes	No	No	No	No	No	No
76	C00029339	(6E)-3,7,11-Trimethyl-1,6,10-dodecatrien-3-ol	High	Yes	No	Yes	No	Yes	No	No
77	C00029350	cis-beta-Farnesene	Low	No	No	Yes	No	Yes	No	No
78	C00029479	3,4-dimethoxybenzoic acid	High	Yes	No	No	No	No	No	No
79	C00029536	4-Methoxybenzoic acid	High	Yes	No	No	No	No	No	No
80	C00029544	4-Terpineol	High	Yes	No	No	No	No	No	No
81	C00029674	alpha-Terpineol	High	Yes	No	No	No	No	No	No
82	C00029763	Aurapten	High	Yes	No	Yes	Yes	Yes	No	No
83	C00030099	Decanal	High	Yes	No	No	No	No	No	No
84	C00030828	Nonadienal	High	Yes	No	No	No	No	No	No
85	C00030880	Octanal	High	Yes	No	No	No	No	No	No
86	C00031258	4(10)-Thujene	Low	Yes	No	No	No	No	No	No
87	C00034600	Methyl anthranilate	High	Yes	No	No	No	No	No	No
88	C00034775	6-Methyl-5-hepten-2-one	High	Yes	No	No	No	No	No	No
89	C00034989	(E)-Ocimene	Low	Yes	No	No	No	No	No	No
90	C00035043	alpha-terpineol acetate	High	Yes	No	No	No	Yes	No	No
91	C00035130	Methyl geranate	High	Yes	No	No	No	No	No	No
92	C00035138	Neryl acetate	High	Yes	No	No	No	No	No	No
93	C00035823	Citronellal	High	Yes	No	No	No	No	No	No
94	C00036308	D-germacrene	Low	No	No	No	No	Yes	No	No
95	C00046607	alpha-Curcumene	Low	No	No	No	No	No	Yes	No
96	C00048263	2,6-Dimethyl-1,3,5,7-octatetraene	Low	Yes	No	No	No	No	No	No
97	C00048304	Acetone	High	No	No	No	No	No	No	No
98	C00048310	2,6-Dimethyl-2,4,6-octatriene	Low	Yes	No	No	No	No	No	No
99	C00048315	alpha-Myrcene	Low	Yes	No	No	No	No	No	No
100	C00048350	Carvyl acetate	High	Yes	No	No	No	Yes	No	No
101	C00048438	Isopropyl alcohol	High	No	No	No	No	No	No	No
102	C00048486	Neo-allo-ocimene	Low	Yes	No	No	No	No	No	No
103	C00048498	n-Phenylformamide	High	High	Yes	No	No	No	No	No
104	C00051735	Synephrine	High	No	No	No	No	No	No	No
105	C00053039	Epoxybergamottin	High	Yes	No	Yes	Yes	Yes	Yes	Yes

(*continued on next page*)

Table 1 (*continued*)

No	Compound ID	Metabolite	GI Absorption	BBB Permeant	P-gp Substrate	CYP1A2 Inhibitor	CYP2C19 Inhibitor	CYP2C9 Inhibitor	CYP2D6 Inhibitor	CYP3A4 Inhibitor
106	C00053122	cis-ocimene	Low	Yes	No	No	No	No	No	No
107	C00053828	Tetrahydrolinalool	High	Yes	No	No	No	No	No	No
108	C00053869	1-Tritriacontanol	Low	No	Yes	No	No	No	No	No
109	C00056187	trans-Carvyl acetate	High	Yes	No	No	No	Yes	No	No
110	C00059951	Linalyl propionate	High	Yes	No	No	No	Yes	No	No
111	C00062142	Malonaldehyde	High	No	No	No	No	No	No	No

centrality, betweenness centrality, and closeness centrality. Fig. 3 illustrates the visual clustering of these hub genes, with nodes color-coded based on their centrality scores. Red nodes such as ESR1, HDAC1, MDM2, and CCND1 represent genes with the highest degree values, indicating their critical roles in protein–protein interactions. These hub genes are likely to be essential regulators in pathways associated with breast cancer. Nodes in orange (e.g., AKT1, AR, BCL2) and yellow (e.g., PIK3CA, KDM1A, HIF1A) show slightly lower, but still significant, centrality values. Blue nodes like HIF1A suggest peripheral yet functionally relevant positions in the network. The right panel further zooms in on the top 10 hub genes to clarify their interaction density. These include key genes implicated in cell proliferation, hormonal response, and apoptosis. Identifying such hub targets enables the prioritization of downstream validation through molecular docking and experimental studies.

The connectivity patterns among these core targets provide critical insights into their cooperative biological roles. ESR1, as the most connected node, reinforces the hormonal axis's importance in breast cancer treatment. The inclusion of AKT1 and PIK3CA emphasizes the involvement of the PI3K/AKT signaling pathway, often dysregulated in breast cancer. HDAC1 and MDM2 play roles in epigenetic regulation and p53 degradation, respectively, highlighting mechanisms of transcriptional control and apoptosis evasion.[46] The presence of BCL2 as a hub gene indicates a role in apoptosis inhibition, which may contribute to cancer cell survival. AR (androgen receptor) appears connected with both hormonal and cell cycle regulators, reflecting its emerging role in certain breast cancer subtypes.[47] CCND1 and KDM1A are linked to cell cycle progression and chromatin remodeling, both crucial for unchecked cellular proliferation. The interconnectedness of these nodes suggests coordinated functional modules rather than isolated signaling events. These observations support the systems biology perspective that *Citrus aurantium* metabolites may target multiple converging points in oncogenic pathways. The extracted hub genes form a tightly integrated regulatory network with potential therapeutic implications.

3.5. Topological characteristics of key target genes in the PPI network

Table 2 summarizes the top 10 key targets selected based on topological parameters within the protein–protein interaction network. These parameters include neighborhood connectivity, closeness centrality, and betweenness centrality, each reflecting different aspects of network influence. ESR1 demonstrated the highest closeness centrality value of 0.9000 and the highest betweenness centrality of 0.2477, indicating its prominent role as a central hub and mediator of communication across the network. MDM2, ranked second, showed high connectivity and centrality values, suggesting a role in regulating multiple neighboring nodes and pathways. HDAC1, AKT1, and CCND1 also showed substantial neighborhood connectivity and closeness, reinforcing their potential regulatory significance in breast cancer. Despite having high neighborhood connectivity, genes like KDM1A and PIK3CA exhibited low or zero betweenness centrality, implying they might serve more localized or peripheral roles. BCL2, involved in apoptosis inhibition, had moderate values across all parameters, supporting its involvement in cancer cell survival. Interestingly, HIF1A and AR both shared identical closeness and betweenness scores, underscoring potential functional collaboration or co-regulation. The convergence of high centrality across multiple metrics in genes like ESR1 and MDM2 strengthens their candidacy for therapeutic targeting. These results provide a quantitative basis for selecting core targets in the subsequent docking and simulation stages.

The significance of these topological metrics lies in how they inform drug target prioritization. Closeness centrality quantifies how quickly a protein can influence others within the network, making ESR1 particularly important for rapid signal propagation. Betweenness centrality highlights the role of a protein as a bridge in communication paths, and high values like that of ESR1 and MDM2 indicate regulatory bottlenecks.

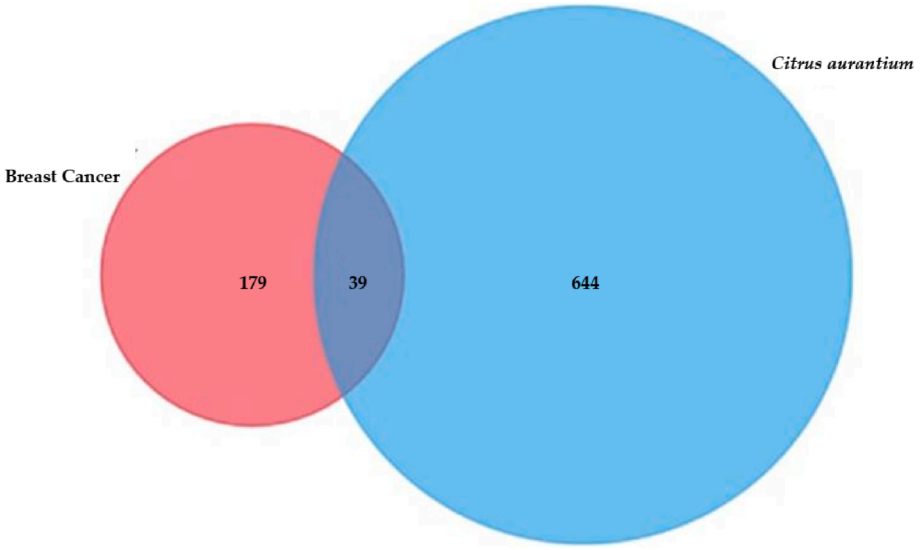


Fig. 1. Venn diagram of overlapping target genes between breast cancer and *Citrus aurantium* metabolites.

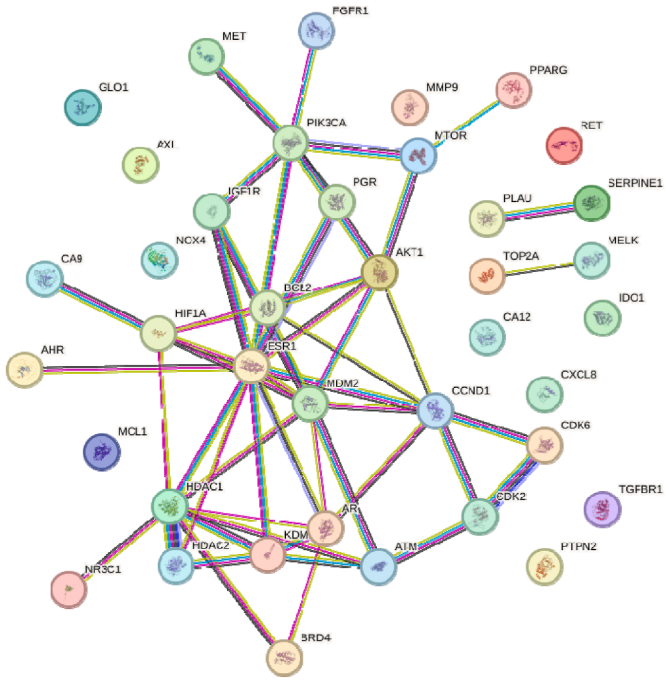


Fig. 2. Protein–protein interaction (PPI) network of overlapping target genes between breast cancer and *Citrus aurantium* metabolites.

High neighborhood connectivity, as observed in PIK3CA and CCND1, reflects a protein's extensive interaction with adjacent nodes, implying robust local influence. While KDM1A and PIK3CA have lower centrality scores, their high connectivity suggests supportive roles within subnetwork clusters. The presence of both hormonal (ESR1, AR) and signaling (AKT1, PIK3CA) targets illustrates the multidimensional nature of *Citrus aurantium's* mechanism in breast cancer. These targets span hormonal, epigenetic, and apoptotic processes, reinforcing the multi-targeted intervention model suggested by network pharmacology. The ranked and structured analysis of targets ensures a rational basis for selecting molecules for further docking studies. Such parameter-based screening enhances the reliability of hub gene identification beyond mere visual interpretation. This approach validates target importance through objective network analytics. These insights collectively support the hypothesis that *Citrus aurantium* metabolites act on a complex, interconnected signaling web involved in breast cancer.

3.6. Functional enrichment analysis of overlapping targets

Enrichment analysis presented in Fig. 4 identifies biological processes such as regulation of programmed cell death, apoptotic signaling, and metabolic control as dominant functions of the overlapping targets. The involvement in positive regulation of cellular processes and response to chemical or organic stimuli suggests active roles in cellular stress adaptation. Other terms, including macromolecule metabolic regulation and control of cell population proliferation, reflect potential influence on tumor maintenance or regression. Molecular function terms like protein kinase activity, transcription factor binding, and nuclear receptor signaling suggest relevance in hormone-regulated cancer pathways. The presence of enzyme binding and catalytic activity further supports these targets' engagement in dynamic biochemical interactions.[48] Within the cellular component category, genes are localized in nuclear structures including nucleoplasm and transcription regulator complexes. These locations align with known activity of many hormone-related oncogenic proteins. The gene count and significance level indicate that multiple targets share similar functional contexts, reinforcing their selection. Enrichment of chromatin-associated complexes implies potential regulation at the epigenetic level. This functional mapping offers justification for focusing molecular docking and simulation efforts on these interconnected pathways.

Additional insights are derived from KEGG pathway enrichment, where targets are clustered in critical cancer-related signaling routes. Several proteins are involved in pathways such as endocrine resistance, prostate cancer, and transcriptional dysregulation, extending the relevance of these compounds beyond breast cancer alone. Other enriched pathways include microRNAs in cancer and proteoglycans in cancer, which often act in cell–cell communication and tumor microenvironment modulation. The prominence of cellular senescence, melanoma, and chronic myeloid leukemia pathways suggests broad therapeutic applicability.[49] Signaling through thyroid hormone and transcription factor-related networks indicates that these targets span diverse cellular control points. The convergence of multiple cancer types among the enriched pathways reveals shared vulnerability points in oncogenesis. Involvement in protein interaction and regulation complexes supports the selection of compounds that bind intracellular targets rather than surface receptors. Targets localized to the nucleus and regulatory

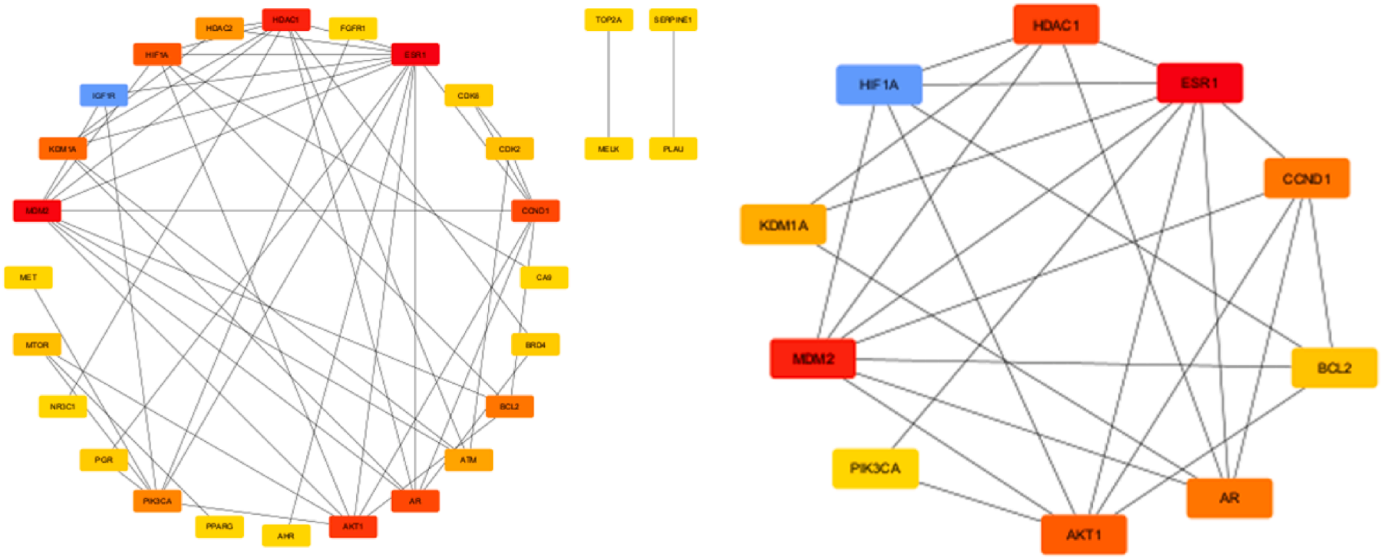


Fig. 3. Visualization of hub genes identified from PPI network.

Table 2
Top 10 key core targets identified based on network topological parameters.

No	Key Core Targets	Neighborhood Connectivity	Closeness Centrality	Betweenness Centrality
1	ESR1	4.75	0.9000	0.2477
2	MDM2	5.43	0.8182	0.0891
3	HDAC1	5.60	0.6923	0.0394
4	AKT1	5.17	0.7500	0.0868
5	CCND1	6.00	0.6923	0.0370
6	AR	5.60	0.6923	0.0394
7	HIF1A	6.00	0.6923	0.0370
8	KDM1A	6.00	0.5625	0.0000
9	BCL2	5.75	0.6000	0.0069
10	PIK3CA	7.00	0.5625	0.0000

chromatin sites are consistent with nuclear modulation mechanisms. These findings align with the polypharmacological nature of natural metabolites, especially those from *Citrus aurantium*. The combination of functional and pathway-based insights reinforces the relevance of selected targets for structure-based drug discovery.

3.7. Molecular docking of Citrus aurantium metabolites with ESR1

From a total of 111 metabolites of *Citrus aurantium* obtained through the KNAPSACK database, only 24 compounds were identified to have predictive interactions with the estrogen receptor alpha (ESR1). This filtering process was based on target prediction results that emphasize proteins linked to breast cancer progression. As shown in Table 3, ESR1 appeared most frequently among the predicted gene targets, making it a key molecular focus. The frequent involvement of ESR1 highlights its central regulatory role in estrogen-mediated signaling in luminal-type breast cancer.[50] Some metabolites also showed interactions with other cancer-related targets such as AKT1 and PIK3CA, suggesting their broader relevance. However, ESR1 was prioritized due to its strong disease linkage and tractable structure for ligand binding. The 24 ESR1-associated metabolites consist mainly of terpenoids and polyphenolic compounds, particularly flavonoid derivatives. These molecules present structural features favorable for interaction with nuclear hormone receptors. The emphasis on ESR1 selection is consistent with the aim of identifying hormone-related therapeutic modulators. Therefore, the screening outcome provides a rational starting point for molecular docking evaluation.

Binding affinity evaluation was conducted through molecular docking simulations using AutoDock Tools 1.5.7. The docking results enabled ranking of the 24 ESR1-binding metabolites based on their binding energy and inhibition constant. As presented in Table 4, seven compounds demonstrated the most promising docking scores and nanomolar to low micromolar inhibitory constants. These top-ranked ligands included 5,7,3′,4′-tetrahydroxyflavone (−8.26 kcal/mol), hesperetin (−8.24 kcal/mol), 4′,5,7,8-tetramethoxyflavone (−7.98 kcal/mol), alpha-copaene (−7.44 kcal/mol), apigenin (−7.37 kcal/mol), 5,7,4′-trimethoxyflavone (−7.40 kcal/mol), and scutellarein 5,6,7,4′-tetramethyl ether (−7.52 kcal/mol). These values indicate favorable binding interactions with ESR1, especially considering the generally accepted threshold of −6.0 kcal/mol for ligand candidacy. Among them, 5,7,3′,4′-tetrahydroxyflavone showed the lowest binding energy and sub-micromolar affinity, supporting its role as a lead compound. Hesperetin and apigenin also stood out with their balance of energy efficiency and predicted bioavailability. The remaining top ligands exhibited consistent scores within a narrow range, underscoring structural similarity and binding potential. As a whole, the docking data indicate strong ligand–receptor interactions for the seven selected candidates. These results serve as the foundation for further interaction and dynamics assessments.

To further validate these docking results, the interaction profiles between the top seven compounds and ESR1 residues were investigated. The interaction maps are detailed in Table 5, showing hydrogen bonds, hydrophobic interactions, and electrostatic forces. 5,7,3′,4′-Tetrahydroxyflavone exhibited four hydrogen bonds with HIS524, GLU353, and MET421, as well as multiple Pi-alkyl and Pi–Pi T-shaped interactions with PHE404 and LEU391. Hesperetin formed hydrogen bonds with ASP351, VAL534, TYR526, and VAL533, complemented by hydrophobic interactions with TRP383, LEU354, and ALA350. Alpha-copaene, although devoid of hydrogen bonds, was stabilized through Pi-alkyl contacts with PRO324, MET537, and TRP360. Apigenin displayed strong binding through hydrogen bonding at ARG394 and GLU353, as well as π-interactions and van der Waals forces. Scutellarein 5,6,7,4′-tetramethyl ether formed mixed electrostatic and hydrophobic contacts with TRP393, GLU353, and ARG394, enhancing its binding profile. 4′,5,7,8-Tetramethoxyflavone shared key interactions with TRP383 and LEU354, showing favorable alignment with conserved ESR1 residues. 5,7,4′-Trimethoxyflavone exhibited similar interaction types, confirming its compatibility with the ESR1 pocket. These interaction characteristics affirm the structural suitability of these compounds as ESR1 ligands. Altogether, the presence of stable contacts with catalytically relevant residues supports further exploration.

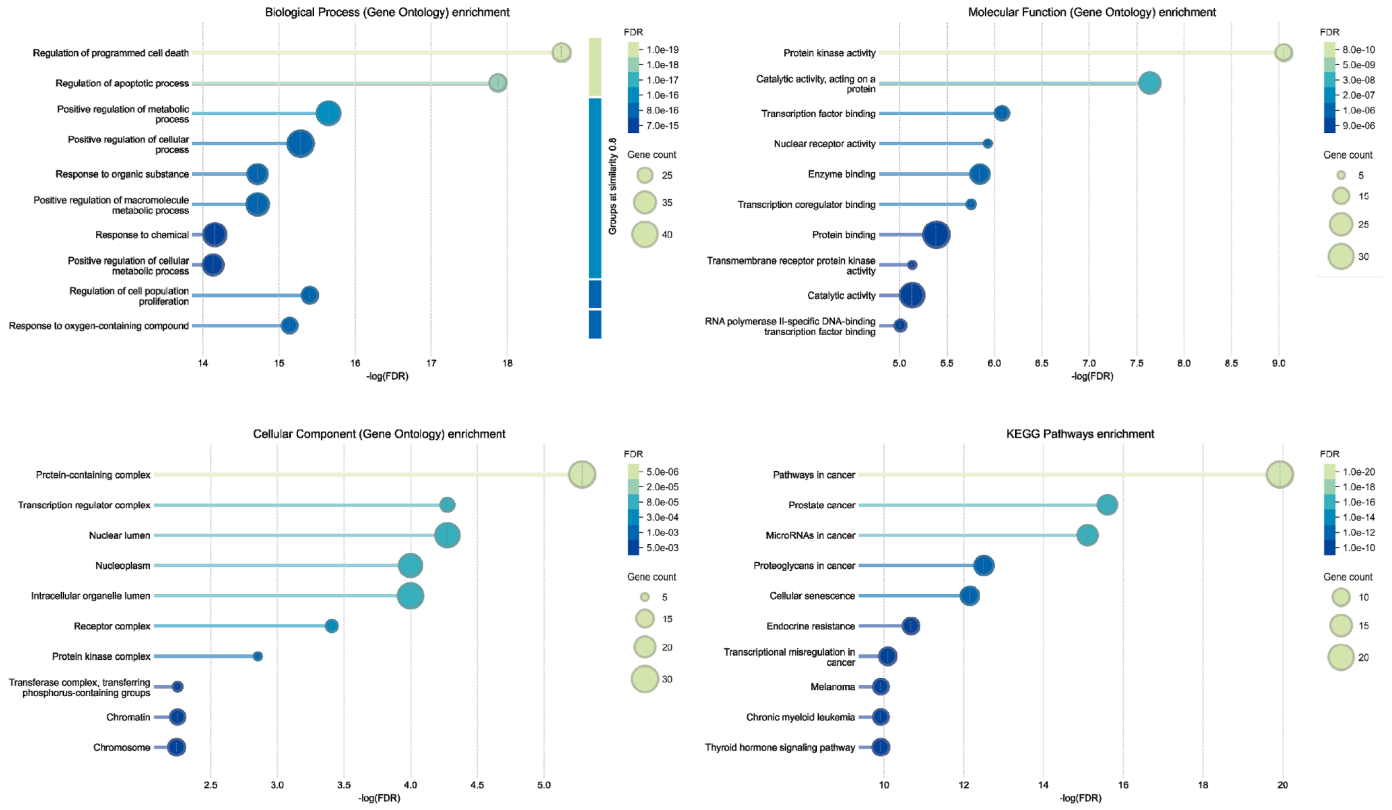


Fig. 4. Gene Ontology (GO) and KEGG pathway enrichment analysis of overlapping targets.

The spatial orientation and molecular surface engagement of the best two compounds, 5,7,3′,4′-tetrahydroxyflavone and hesperetin, were visualized through docking pose analysis. As shown in Fig. 5, the top panel illustrates the binding of 5,7,3′,4′-tetrahydroxyflavone to ESR1's ligand-binding domain. The planar flavone scaffold allowed this molecule to form extended π-conjugation with aromatic residues such as PHE404 and LEU387. A network of four hydrogen bonds stabilized its orientation within the hydrophobic pocket, including contributions from HIS524 and GLU353. Hydrophobic interactions further supported docking conformation, with residues like LEU391 and ALA350 reinforcing the binding. The ligand's position was surrounded by favorable electrostatic regions, suggesting enhanced complementarity. Hesperetin adopted a bent conformation, accommodating the cavity shape of ESR1. This compound engaged TYR526, ASP351, and VAL533 in multiple hydrogen bond formations. Its phenolic groups contributed to both polar and non-polar interactions across the pocket surface. The consistent interaction geometry confirms the docking reliability for both ligands.

While 5,7,3′,4′-tetrahydroxyflavone showed the highest docking score, hesperetin demonstrated an equally favorable interaction pattern with essential ESR1 residues. The comparative analysis reveals that hesperetin's flexibility enabled it to fit tightly within the receptor's binding groove. Although hesperetin formed fewer hydrogen bonds than 5,7,3′,4′-tetrahydroxyflavone, it compensated with a broader spectrum of hydrophobic contacts. Residues such as TRP383, LEU536, and LEU354 anchored the ligand via van der Waals forces, enhancing its spatial occupancy. The electron-rich regions on hesperetin's B-ring allowed interaction with polar residues through π-stacking. This binding landscape supports hesperetin's potential as an ESR1 modulator, especially for hormone-responsive breast cancers. The visualization reinforces the notion that structural orientation and interaction distribution are critical for ligand efficacy. Furthermore, the conserved residue interactions across both ligands indicate key anchoring points on ESR1. This dual analysis of docking score and interaction quality helps refine candidate prioritization. These observations align with the hydrogen bonding and Pi-system contributions identified in the interaction profile.

The integration of gene-target prediction, docking scores, molecular interaction data, and structural modeling demonstrates the potential of *Citrus aurantium* metabolites as ESR1-targeted ligands. The information consistently points to a subset of polyphenolic compounds with robust pharmacological promise. Notably, 5,7,3′,4′-tetrahydroxyflavone and hesperetin show strong binding, stable interaction networks, and spatial compatibility with ESR1's binding site. These characteristics suggest their functional capacity as selective estrogen receptor modulators. Additional compounds such as apigenin, alpha-copaene, and scutellarein also merit further investigation due to their favorable docking metrics and interaction profiles. This multi-layered computational approach provides a rigorous filter for experimental validation. By narrowing candidates through network pharmacology and docking simulations, the study supports natural-product-based drug discovery against breast cancer. Continued research will involve dynamic simulation to assess conformational stability. These findings underscore the therapeutic potential of *Citrus aurantium* and support its development in hormone-targeted oncology.

3.8. *Molecular dynamics analysis of ESR1 complexes*

The RMSD results illustrated in Fig. 6 provide insight into the stability of ESR1 when complexed with different ligands across 300 ns. The ESR1–hesperetin system displayed the highest deviations, fluctuating near 0.40–0.45 nm, suggesting greater conformational adjustments. In contrast, the complex with the native ligand maintained the lowest RMSD values, stabilizing close to 0.30 nm throughout the simulation. The trajectory of 5,7,3′,4′-tetrahydroxyflavone revealed intermediate stability, averaging between 0.35 and 0.38 nm. Importantly, all systems equilibrated after ~100 ns, indicating that ESR1 maintained its overall fold despite ligand binding. The persistent low RMSD of the native ligand reflects its evolutionary fit with the receptor's binding cavity. The 5,7,3′,4′-tetrahydroxyflavone showed slightly higher variability,

Table 3
Predicted target genes of *Citrus aurantium* metabolites and their associations with breast cancer-related genes.

No	Metabolite	Target Genes Prediction	Target Genes Linked to Breast Cancer
1	cis-p-Menth-2-en-1-ol	AR, RORC, NPC1L1, RORA, SHBG, CA2, CA1, CA4, SQLE, NR1H3, CYP19A1, PTPN1, POLB, NR1I3, TRPM8, SREBF2, BCHE, CHRM2, ACHE, SLC6A4, NR3C1, DRD2, ESR1, PPARG, PPARA, PPARD	ESR1
2	trans-p-Menth-2-en-1-ol	AR, TRPM8, SHBG, NPC1L1, RORA, CA2, CA1, CA4, CYP19A1, CHRM2, SQLE, BCHE, NR1H3, SLC6A4, NR3C1, NR1I3, SREBF2, SLC6A2, DRD2, ESR1, TRPV3, ACHE, ESR2, SRD5A2, CYP17A1, PPARA, PPARD, CHRM4	ESR1
3	alpha-Thujene	PPARA, CNR2, NR1I3, FAAH, TRPV1, AR, CYP19A1, ESR1, CHRM2, SLC6A2, SLC6A4, CYP2C19	ESR1
4	5,7,3′,4′-Tetrahydroxyflavone	NOX4, AKR1B1, CDK5R1, CDK5, XDH, MAOA, FLT3, CA2, CCNB3, CDK1, CCNB1, CCNB2, ALOX5, ADORA1, CA7, GLO1, APP, SYK, GSK3B, PARP1, TTR, MMP9, CA12, MMP2, CA4, MMP12, CD38, CYP1B1, ABCG2, AKR1B10, TNKS2, TNKS, TOP1, ARG1, PTPRS, ABCC1, HSD17B1, ACHE, CDK6, ABCB1, HSD17B2, CYP19A1, ESR2, ADORA2A, CSNK2A1, ALOX15, ALOX12, ESR1, PTGS2, CFTR, AMY1A, GRK6, CA1, CA9, CDK2, TERT, CDK1, TYR, AHR, ESRRA, GPR35, AVPR2, IGF1R, EGFR, F2, PIM1, AURKB, DRD4, MPO, PIK3R1, DAPK1, PYGL, SRC, PTK2, KDR, MMP13, MMP3, CA3, PLK1, CA6, PKN1, CA14, MET, NEK2, CXCR1, CAMK2B, ALK, AKT1, NEK6, PLA2G1B, CA5A, BACE1, AXL, NUAK1, AKR1C2, AKR1C1, AKR1C3, AKR1C4, CA13, AKR1A1, PFKFB3, PLG, KDM4E, AR	ESR1, AKT1
5	alpha-Pinene	PPARA, CNR2, ACHE, FAAH, TRPV1, AR, CYP19A1, ESR1, CHRM2, SLC6A2, SLC6A4, CYP2C19, BCHE, PTPN1	ESR1
6	cis-Sabinene hydrate	CA2, CA1, CA4, TRPM8, AR, CDC25A, CDC25B, NR1I3, NR1H4, GPRAB1, SHH, ESR1, ESR2, SHBG, UGT2B7, NR1H3, POLA1, NPC1L1, HSD11B1, NR3C1, DRD2, G6PD, GABBR1, NR3C2, PGR, IDO1	ESR1
7	3-Carene	PPARA, CNR2, FAAH, TRPV1, AR, CYP19A1, ESR1, CHRM2, SLC6A2, SLC6A4, CYP2C19	ESR1
8	Citronellol	AR, CYP19A1, SQLE, SLC6A2, BCHE, HMGCR, CHRM2, CYP2C19, NR1I3, ESR1, SLC6A4, HSD11B1, EPHX2, CYP17A1, PTGS2, KCNA3, SREBF2, NPC1L1, FABP4, PPARA, TERT, FABP3, FABP5, PPARD, FABP1, CYP51A1, PTGS1, JAK1, JAK2, ACHE, SCD, KCNH2	ESR1
9	Eriodictyol	CA7, CA12, CA4, CYP1B1, CYP19A1, PTGS1, ABCC1, HSD17B1, SHBG, CBR1, ESR2, ESR1, MAOB, TAS2R31, ADORA1, ADORA3, ABCG2, MMP13, AKR1C3, MMP12, PLA2G1B, KLK1, KLK2, APP, GRM5, CES1, PPARG, CES2, MAPT, CA2, CA1, BACE1, POLB, CDK5R1, CDK5, KIT, SRC, KDR, FGFR1, MET, PLA2G2A, PLA2G5, PLA2G10, EDNRA, SNCA, CA6, CA5A, CHRNA7, DYRK1A, CA9, ABCB1, ACHE, CA3, CA13, CA5B, KCNH2, ST3GAL3, FUT7, FUT4, RXRA, TERT, FFAR1, NOX4, MMP2, BCL2, IGFBP3, LCK, SYK, AKR1B1, HIF1A, CTSB, NQO2, CLK1, DYRK1B, MMP9, IGF1R, INSR, ODC1, AKT1, TOP1	ESR1, AKT1
10	Hesperetin	CA7, CA12, CA4, CYP1B1, CYP19A1, TAS2R31, ADORA1, ADORA3, ABCG2, HSD17B1, ESR2, ESR1, MAOB, ABCC1, SHBG, CBR1, MMP13, PTGS1, BACE1, MMP12, GRM5, SRC, AKR1C3, PLA2G1B, KLK1, KLK2, CA3, CHRNA7, TERT, CA2, CA1, CA6, CA5A, POLB, SERPINE1, APP, PLA2G5, PLA2G10, PLG, NOX4, CA13, CA5B, ACHE, GUSB, CES1, SLC5A2, CES2, RXRA, KDR, GRM2, AKR1B1, CDK1, CCNB1, CCNE1, CDK2, DUSP3, NTRK1, AURKA, CA9, TOP1, DNMT1, PGD, ST3GAL3, FUT7, FUT4, STAT1, SQLE, FFAR1, PIM1, PIM2, PIM3, MMP2, IGF1R, MMP9, ODC1, PARP1, DNM1, TNKS2, TNKS, MET, DYRK1A, ABCB1, PPARG, MAP4K4, PLA2G2A, CDK2, CCNA1, CCNA2, PRMT1, HSD17B2, EDNRA, BCL2	ESR1
11	Diosmetin	ABCC1, CYP1B1, XDH, CA2, CA7, CA12, CA4, AKR1B1, CDK5R1, CDK5, CCNB3, CDK1, CCNB1, CCNB2, ARG1, PLG, PTPRS, ABCB1, APP, NOX4, MAOA, FLT3, ALOX5, ADORA1, GLO1, GSK3B, MMP9, MMP2, ABCG2, SYK, PARP1, TTR, MMP12, CD38, AKR1B10, TNKS2, TNKS, TOP1, PIM1, ADORA2A, ACHE, CDK6, CYP19A1, PLA2G2A, TERT, ESR1, ESR2, CSNK2A1, HSD17B1, CBR1, OPRD1, IGF1R, EGFR, ALOX15, ALOX12, HSD17B2, CA1, CA9, KIT, CDK2, F2, CDK1, PTGS2, CFTR, AVPR2, AURKB, DRD4, MPO, PIK3R1, DAPK1, PYGL, SRC, PTK2, KDR, MMP13, MMP3, CA3, PLK1, CA6, PKN1, CA14, MET, NEK2, CXCR1, CAMK2B, ALK, AKT1, NEK6, PLA2G1B, CA5A, BACE1, AXL, NUAK1, AKR1C2, AKR1C1, AKR1C3, AKR1C4, CA13, AKR1A1, MCL1, GPR35, ST6GAL1, AMY1A, GRK6	ESR1, AKT1
12	Tyramine	AAR1, DRD2, DRD3, DRD1, DRD4, KDM4E, DRD5, MTNR1A, MTNR1B, SLC6A2, SLC6A3, SLC6A4, ADRA2A, ADRA2C, HTR3A, HTR6, HTR2A, GAPDH, NMUR2, AR, ESR1, ESR2, ESRRG, CHRNA7, ADRA2B, MIF, HTR2B, HTR2C, HTR1D, ADORA3, HRH1, SHBG, GABRA1 GABRB2 GABRG2	ESR1
13	alpha-Copaene	PPARA, CNR2, AR, CYP19A1, ESR1, CHRM2, SLC6A2, SLC6A4, CYP2C19, BCHE, PTPN1, NR1I3, FAAH, TRPV1	ESR1
14	Apigenin	NOX4, AKR1B1, CDK5R1 CDK5, XDH, MAOA, FLT3, CYP19A1, ESR1, CCNB3 CDK1 CCNB1 CCNB2, ACHE, ADORA1, PTGS2, ESR2, CDK6, ADORA2A, SYK, GSK3B, ABCC1, HSD17B1, TTR, CSNK2A1, CFTR, CYP1B1, ABCG2, AKR1B10, TNKS2, TNKS, ALOX5, PARP1, CA2, CA7, CA12, ABCB1, CA4, ALOX12, PTPRS, GLO1, APP, MMP9, MMP2, MMP12, CD38, TOP1, ARG1, ESRRA, PFKFB3, ALOX15, AMY1A, GRK6, TYR, HSD17B2, AHR, CA1, CA9, CBR1, AR, TERT, PIM1, EGFR, CDK1, KDM4E, LCK, AURKB, NAE1, TBXAS1, IGF1R, KDR, PLK1, MET, ALK, AXL, BCHE, ADORA3, CDK2, HTR2C, GPR35, DAPK1, MPG, SLC22A12, ST6GAL1, F2, PLG, AVPR2, DRD4, MPO, PIK3R1, PYGL, SRC, PTK2, MMP13, MMP3, CA3, CA6, PKN1, CA14, NEK2, CXCR1, CAMK2B, AKT1, NEK6	ESR1, AKT1
15	5,7,4′-Trimethoxyflavone	ABCG2, ADORA1, ADORA3, CYP1B1, ABCB1, SYK, ADORA2A, PTGS2, CYP19A1, CSNK2A1, TNKS, AKR1B1, GSK3B, PIM1, AR, KIT, HSD17B1, TNKS2, CDK5R1, CDK5, ACHE, CA2, CA1, CCNB3, CDK1, CCNB1, CCNB2, FLT3, CA7, CA12, MAOA, ESR1, ABCC1, CA9, ALOX5, MAOB, ESR2, CFTR, CD38, PARP1, CA4, OPRD1, TTR, LCK, MMP12, NOX4, PTPRS, AMY1A, PLG, CBR1, MMP2, APP, MMP9, CDK1, CDK6, HSD17B2, AKR1B10, KDR, GLO1, ARG1, EGFR, ALOX12, AURKB, MET, TERT, XDH, MCL1, PFKFB3, PLA2G2A, OPRM1, MMP13, NAE1, SIGMAR1, PIK3CG, ALK, ALOX15, ODC1, PLK1, TYR, CA6, CA13, DRD4, NOS2, IGF1R, INSR, BACE1, CDK2, AKT1, ALDH2, IKBKB, SRC, PTK2, PTPN1, GPR35, F2, CYP1A1, KDM4E, AKR1C3, PPARG, ABL1, BCHE, MPG, NEK2, AXL	ESR1, AKT1
16	Scutellarein 5,6,7,4′-tetramethyl ether	OPRD1, ADORA2A, ADORA1, ADORA3, CYP1B1, AKR1B1, ABCG2, FLT3, KIT, PIM1, ABCB1, PTGS2, TERT, PTPRS, OPRM1, PLG, SYK, CYP19A1, ALOX5, GSK3B, NOX4, ACHE, HSD17B1, TNKS2, TNKS, AMY1A, GRK6, CDK5R1, CDK5, CDK1, CCNB3, CCNB1, CCNB2, CSNK2A1, AR, APP, NOS2, ESR2, MAOA, PARP1, CFTR, PFKFB3, ESR1, MMP9, CD38, ABCC1, CA7, GLO1, CA12, TOP1, ARG1, CA1, CA9, MMP2, SIGMAR1, HSD17B2, CA2, DRD4, KDR, PLK1, MET, MAOB, MMP13, MMP12, SRC, IGF1R, AKR1B10, AURKB, XDH, ODC1, EGFR, ALK, IKBKB, CDK6, PLA2G2A, DRD2, LCK, ALOX15, AHR, ESRRA, KDM4E, NTRK2, NAE1, TTR, INSR, PIK3CG, MCL1, TUBB1, AKT1, PTK2, BACE1, AXL, GPR35, MPO, PIK3R1, DAPK1, CA3, PKN1, CA13, NEK6, APEX1, NUAK1, AKR1C1	ESR1, AKT1
17	beta-Phellandrene	AR, CYP19A1, ESR1, ESR2, PPARA, CNR2	ESR1
18	2,4(8)-p-Menthadiene	AR, CYP19A1, ESR1, ESR2, RBP4, PPARA, CNR2	ESR1
19	4′,5,7,8-Tetramethoxyflavone	AKR1B1, OPRD1, PTGS2, ABCG2, OPRM1, NOS2, KIT, ADORA3, ADORA1, ADORA2A, ALOX5, CYP1B1, PIM1, ABCB1, PFKFB3, MCL1, TERT, FLT3, TNKS, SYK, CYP19A1, TNKS2, HSD17B2, HSD17B1, CYP1A1, IKBKB,	ESR1, AKT1, PIK3CA

(*continued on next page*)

Table 3 (*continued*)

No	Metabolite	Target Genes Prediction	Target Genes Linked to Breast Cancer
		EGFR, PARP1, CA2, CA12, NOX4, CA7, APP, ALK, CYP1A2, GSK3B, KDR, ACHE, PLK1, ABCC1, AR, MAOA, IGF1R, INSR, PTPRS, AURKB, MET, ODC1, CDK5R1, CDK5, PIK3CG, CCNB3, CDK1, CCNB1, CCNB2, CSNK2A1, CA4, CA1, CA9, AMY1A, DRD4, CA6, CA13, AKT1, GPR35, BACE1, CD38, PLG, SRC, MMP13, ESR1, TTK, TTR, PTK2, XDH, F2, AXL, BCHE, ESR2, CFTR, MPG, ALOX12, CDK2, MMP9, NTRK2, AKR1C3, MMP2, MMP3, ICAM1, SELE, GLO1, TOP1, ARG1, NEK2, APEX1, AKR1C1, AKR1C4, LCK, PIK3CA, MAPK9, CBR1, MAOB, PYGL	
20	4-Terpineol	AR, CYP19A1, CA2, CA1, CA4, RORC, SREBF2, NPC1L1, NR1H3, HMGCR, TRPM8, ESR2, CHRM2, CYP17A1, PTPN1, RORA, SQLE, DRD2, SLC6A4, CYP51A1, PPARA, PPARD, G6PD, ESR1, ACHE, ADRA2C, HSD17B2, SHBG, SLC6A2, NR3C1, NR3C2, BCHE, PTPRF, PTPN2, PLA2G1B, ACP1, AKR1B10	ESR1
21	alpha-Terpineol	AR, CYP19A1, CA2, CA1, CA4, TRPM8, CHRM2, SLC6A4, NR1H3, PTPN1, NR1I3, SREBF2, NPC1L1, BCHE, ESR1, SQLE, ACHE, CYP51A1, SLC6A2, DRD2, CYP17A1, ESR2, CYP2C19, NR3C2, PTPRF, PTPN2, PLA2G1B, ACP1, AKR1B10, SIGMAR1, NR3C1, TRPV3, ATP12A, PTPN6, SHBG, FABP4, PPARA, FABP3, FABP5, PPARD, FABP1, RORA, HMOX1, HMGCR, CD81, PGR, G6PD, SCD, ADRA2C, HSD11B1, SLC6A3	ESR1
22	Decanal	CA2, CA1, CYP19A1, AR, NR1I3, CA4, CES1, CES2, ADH1A, ADH1B, ADH1C, ADH7, HLCS, SRD5A1, PTGS1, PGR, MTNR1A, MTNR1B, ACHE, MMP13, MMP1, MMP8, MAOB, GRM1, ALOX5, CTSK, ALOX15, CYP2C19, PAOX, CNR2, PARP1, P2RX7, THRB, MAOA, PIM1, ROCK2, PIM2, PIM3, DBF4, CDC7, NQO2, ESR1, PTGS2, ESR2	ESR1
23	Tetrahydrolinalool	TRPM8, CA2, CA1, CA4, AR, SHBG, UGT2B7, ESR1, ESR2, HSD11B1, IDO1, CDC25A, NR3C2, PGR, PTGS2, CDC25B, SIGMAR1, NR3C1, NR1I3, TRPV3, HSD17B2, NR1H4, NPC1L1, CYP19A1, SLC6A4, JAK1, JAK2, CHRM4, CHRM2, OPRM1, OPRD1, OPRK1, KCNH2, GPBAR1, CNR2, PER2, CYP17A1, HIF1A, ALOX5, SLC18A3, SCN5A, SCN9A, HMOX1, ADRA1A, PSEN2, PSENEN, NCSTN, APH1A, PSEN1, APH1B, ADRA2C, LIPA, TRPV1, KCNA5, EIF2AK1, PABPC1	ESR1
24	1-Tritriacontanol	TRPM8, CA2, CA1, CA4, AR, ESR1, ESR2, SHBG, CDC25A, CDC25B, NR1I3, NR1H4, UGT2B7, GPBAR1, SHH, HSD11B1, POLA1, NPC1L1	ESR1

Table 4
Binding energy and inhibition constant of selected *Citrus aurantium* metabolites.

No	Metabolite	Canonical SMILES	Binding Energy (kcal/mol)	Inhibition Constant
1	cis-p-Menth-2-en-1-ol	CC(C)[C@H]1C=C[C@](C) (O)CC1	−6.43	19.32 μM (micromolar)
2	trans-p-Menth-2-en-1-ol	CC(C)[C@H]1C=C[C@@](C) (O)CC1	−5.75	61.20 μM (micromolar)
3	alpha-Thujene	CC1=CCC2(C(C)C)CC12	−5.24	143.67 μM (micromolar)
4	5,7,3′,4′-Tetrahydroxyflavone	O = c1cc(-c2ccc(O)c(O)c2)oc2cc(O)cc(O)c12	−8.26	880.06 nM (nanomolar)
5	alpha-Pinene	CC1=CCC2CC1C2(C)C	−5.81	54.73 μM (micromolar)
6	cis-Sabinene hydrate	CC(C)[C@]12CC[C@@](C) (O)[C@H]1C2	−6.41	20.07 μM (micromolar)
7	3-Carene	CC1=CCC2C(C1)C2(C)C	−5.06	196.35 μM (micromolar)
8	Citronellol	CC(C)=CCCC(C)CCO	−5.12	177.02 μM (micromolar)
9	Eriodictyol	O=C1C[C@@H](c2ccc(O)c(O)c2)Oc2cc(O)cc(O)c21	−6.71	12.08 μM (micromolar)
10	Hesperetin	COc1ccc([C@@H]2CC(=O)c3c(O)cc(O)cc3O2)cc1O	−8.24	908.05 nM (nanomolar)
11	Diosmetin	COc1ccc(-c2cc(=O)c3c(O)cc(O)cc3o2)cc1O	−6.70	12.20 μM (micromolar)
12	Tyramine	NCCc1ccc(O)cc1	−4.97	229.01 μM (micromolar)
13	alpha-Copaene	CC1=CCC2C3C(C(C)C)CC[C@@]2(C)C13	−7.44	3.54 μM (micromlar)
14	Apigenin	O = c1cc(-c2ccc(O)cc2)oc2cc(O)cc(O)c12	−7.37	3.98 μM (micromlar)
15	5,7,4′-Trimethoxyflavone	COc1ccc(-c2cc(=O)c3c(OC)cc(OC)cc3o2)cc1	−7.40	3.76 μM (micromlar)
16	Scutellarein 5,6,7,4′-tetramethyl ether	COc1ccc(-c2cc(=O)c3c(OC)c(OC)c(OC)cc3o2)cc1	−7.52	3.06 μM (micromlar)
17	beta-Phellandrene	C=C1C=CC(C(C)C)CC1	−5.84	52.75 μM (micromlar)
18	2,4(8)-p-Menthadiene	CC(C) = C1C=CC(C)CC1	−6.04	37.59 μM (micromlar)
19	4′,5,7,8-Tetramethoxyflavone	COc1ccc(-c2cc(=O)c3c(OC)cc(OC)c(OC)c3o2)cc1	−7.98	1.41 μM (micromolar)
20	4-Terpineol	CC1=CCC(O) (C(C)C)CC1	−6.01	39.08 μM (micromolar)
21	alpha-Terpineol	CC1=CCC(C(C) (C)O)CC1	−6.20	28.66 μM (micromolar)
22	Decanal	CCCCCCCCCC=O	−4.50	503.25 μM (micromolar)
23	Tetrahydrolinalool	CCC(C) (O)CCCC(C)C	−5.25	142.22 μM (micromolar)
24	1-Tritriacontanol	CCCCCCCCCCCCCCCCCCCCCCCCCCCCCCCCCO	−5.44	103.40 μM (micromolar)

particularly beyond 200 ns, reflecting potential conformational rearrangements. Hesperetin, although producing higher displacements, still reached a plateau and remained dynamically stable until 300 ns. These differences emphasize that stability arises not only from minimized deviations but also from the ability to equilibrate. Furthermore, the RMSD outcomes suggest hesperetin maintains a flexible yet acceptable mode of interaction with ESR1.

As shown in the RMSF profile (Fig. 7), residue-level dynamics of ESR1 varied slightly depending on the bound ligand. Overall fluctuations for all systems remained below 0.3 nm, indicating structural conservation. Notable peaks were detected at the C-terminal region, particularly residues 525–550, which are naturally flexible. Hesperetin induced slightly higher fluctuations at residues around PHE404 and LEU525, reflecting localized mobility. By contrast, the native ligand and 5,7,3′,4′-tetrahydroxyflavone maintained more restrained residue movements in these segments. Binding pocket residues such as GLU353 and HIS524 were consistently stable, confirming their central role in ligand anchoring. The presence of 5,7,3′,4′-tetrahydroxyflavone introduced more pronounced deviations at residues LEU346, THR347, LEU387, and HIS524. Meanwhile, hesperetin caused only small shifts at key residues, which may favor its pharmacophoric fit. The similar RMSF patterns across all systems demonstrate that ESR1 retains its secondary structure despite ligand differences. Thus, RMSF data support that hesperetin binding minimizes conformational perturbations while sustaining overall stability.

Analysis of protein compactness through radius of gyration plots revealed that the ESR1–native ligand complex was the most compact, averaging 1.84–1.86 nm. The 5,7,3′,4′-tetrahydroxyflavone system showed slightly higher values around 1.85–1.87 nm, while hesperetin remained the least compact at ~1.88–1.90 nm. These findings indicate differential effects of ligands on ESR1 compactness. The SASA profiles (Fig. 8) showed 5,7,3′,4′-tetrahydroxyflavone consistently exposed more

Table 5
Molecular interactions between *Citrus aurantium* metabolites and ESR1 residues.

No	Metabolite	Interacting Residue	Distance (Å)	Category	Types
1	5,7,3′,4′-Tetrahydroxyflavone	HIS524	3.28037	Hydrogen Bond	Conventional Hydrogen Bond
		GLU353	1.86881	Hydrogen Bond	Conventional Hydrogen Bond
		GLU353	1.80779	Hydrogen Bond	Conventional Hydrogen Bond
		MET421	2.37364	Hydrogen Bond	Conventional Hydrogen Bond
		ILE424	3.58282	Hydrophobic	Pi-Sigma
		PHE404	5.65238	Hydrophobic	Pi–Pi T-Shaped
		MET421	4.85962	Hydrophobic	Pi-Alkyl
		ALA350	5.17122	Hydrophobic	Pi-Alkyl
		LEU387	4.44208	Hydrophobic	Pi-Alkyl
		LEU391	4.70673	Hydrophobic	Pi-Alkyl
2	Hesperetin	ASP351	1.81767	Hydrogen Bond	Conventional Hydrogen Bond
		VAL533	3.04930	Hydrogen Bond	Conventional Hydrogen Bond
		VAL534	1.94135	Hydrogen Bond	Conventional Hydrogen Bond
		TYR526	1.80682	Hydrogen Bond	Conventional Hydrogen Bond
		LEU536	3.36084	Hydrophobic	Pi-Sigma
		TRP383	4.89290	Hydrophobic	Pi–Pi Stacked
		TRP383	3.80061	Hydrophobic	Pi–Pi Stacked
		ALA350	4.45061	Hydrophobic	Alkyl
		LEU354	3.54997	Hydrophobic	Alkyl
		MET537	5.46141	Hydrophobic	Alkyl
		LEU387	3.78006	Hydrophobic	Alkyl
		TRP383	4.64705	Hydrophobic	Pi-Alkyl
		ALA350	5.49952	Hydrophobic	Pi-Alkyl
		LEU354	4.28577	Hydrophobic	Pi-Alkyl
		LEU536	5.46981	Hydrophobic	Pi-Alkyl
3	Alpha-Copaene	PRO324	4.85242	Hydrophobic	Alkyl
		PRO324	4.02902	Hydrophobic	Alkyl
		MET357	4.20668	Hydrophobic	Alkyl
		PRO324	4.07003	Hydrophobic	Alkyl
		MET357	4.47401	Hydrophobic	Alkyl
		ILE386	5.04150	Hydrophobic	Alkyl
		LYS449	4.82240	Hydrophobic	Alkyl
		TRP360	3.63782	Hydrophobic	Pi-Alkyl
		TRP360	3.53199	Hydrophobic	Pi-Alkyl
4	Apigenin	ARG394	2.91772	Hydrogen Bond	Conventional Hydrogen Bond
		GLU353	1.79032	Hydrogen Bond	Conventional Hydrogen Bond
		LEU387	3.94584	Hydrophobic	Pi-Sigma
		MET343	5.87147	Other	Pi-Sulfur
		LEU346	4.80570	Hydrophobic	Pi-Alkyl
		LEU346	5.33120	Hydrophobic	Pi-Alkyl
		MET421	4.83305	Hydrophobic	Pi-Alkyl
		ILE424	5.32856	Hydrophobic	Pi-Alkyl
		ALA350	5.16561	Hydrophobic	Pi-Alkyl
		LEU391	4.58322	Hydrophobic	Pi-Alkyl
5	5,7,4′-Trimethoxyflavone	PRO325	2.88649	Hydrogen Bond	Carbon Hydrogen Bond
		ARG394	4.17939	Electrostatic	Pi-Cation
		LYS449	4.17571	Hydrogen Bond; Electrostatic	Pi-Cation; Pi-Donor Hydrogen Bond
		GLU353	3.08737	Electrostatic	Pi-Anion
		HIS356	3.95610	Hydrophobic	Pi-Sigma
		TRP393	4.60042	Hydrophobic	Pi–Pi T-shaped
		PHE445	5.84533	Hydrophobic	Pi–Pi T-shaped
		ARG394	4.31753	Hydrophobic	Alkyl
		PRO324	4.84860	Hydrophobic	Alkyl
		PRO325	4.01546	Hydrophobic	Alkyl
		LEU327	3.75149	Hydrophobic	Alkyl
		PRO324	4.69801	Hydrophobic	Alkyl
		MET357	3.55893	Hydrophobic	Alkyl
		ILE386	4.65760	Hydrophobic	Alkyl
		TRP360	4.78451	Hydrophobic	Pi-Alkyl
		TRP393	4.12093	Hydrophobic	Pi-Alkyl
		TRP393	5.47560	Hydrophobic	Pi-Alkyl
		PRO324	4.00424	Hydrophobic	Pi-Alkyl
		PRO324	3.79810	Hydrophobic	Pi-Alkyl
		ILE326	5.11573	Hydrophobic	Pi-Alkyl
		ARG394	4.71664	Hydrophobic	Pi-Alkyl
6	Scutellarein 5,6,7,4′-tetramethyl ether	LYS449	2.91900	Hydrogen Bond	Conventional Hydrogen Bond
		GLY390	3.27795	Hydrogen Bond	Carbon Hydrogen Bond
		ILE386	3.23297	Hydrogen Bond	Carbon Hydrogen Bond
		GLU353	3.09861	Hydrogen Bond	Carbon Hydrogen Bond
		ARG394	4.05520	Electrostatic	Pi-Cation
		ARG394	4.30279	Electrostatic	Pi-Cation
		GLU323	4.43387	Electrostatic	Pi-Anion
		GLU353	3.37133	Electrostatic	Pi-Anion
		TRP393	4.31978	Hydrophobic	Pi–Pi T-shaped

(*continued on next page*)

Table 5 (*continued*)

No	Metabolite	Interacting Residue	Distance (Å)	Category	Types
		TRP393	4.42007	Hydrophobic	Pi-Alkyl
		TRP393	5.21251	Hydrophobic	Pi-Alkyl
		PRO324	4.53341	Hydrophobic	Pi-Alkyl
		PRO324	3.82520	Hydrophobic	Pi-Alkyl
		ILE326	5.00265	Hydrophobic	Pi-Alkyl
		ARG394	4.75292	Hydrophobic	Pi-Alkyl
7	4′,5,7,8-Tetramethoxyflavone	CYS530	3.10286	Hydrogen Bond	Conventional Hydrogen Bond
		GLU380	3.76730	Hydrogen Bond	Carbon Hydrogen Bond
		ASP351	3.61145	Electrostatic	Pi-Anion
		ASN532	3.84048	Hydrogen Bond	Pi-Donor Hydrogen Bond
		LEU536	3.65867	Hydrophobic	Pi-Sigma
		TRP383	3.63629	Hydrophobic	Pi-Sigma
		TRP383	3.41091	Hydrophobic	Pi-Sigma
		CYS530	5.30084	Other	Pi-Sulfur
		CYS530	5.39390	Other	Pi-Sulfur
		TRP383	5.85891	Hydrophobic	Pi–Pi Stacked
		TRP383	5.74471	Hydrophobic	Pi–Pi Stacked
		TRP383	4.59410	Hydrophobic	Pi–Pi Stacked
		TRP383	4.08734	Hydrophobic	Pi–Pi Stacked
		ALA350	3.42416	Hydrophobic	Alkyl
		ALA350	4.08010	Hydrophobic	Alkyl
		LEU536	5.30255	Hydrophobic	Alkyl
		LEU525	4.88125	Hydrophobic	Alkyl
		CYS530	4.61305	Hydrophobic	Alkyl
		LEU354	3.72596	Hydrophobic	Alkyl
		LEU387	4.46990	Hydrophobic	Alkyl
		TRP383	5.41392	Hydrophobic	Pi-Alkyl
		TRP383	4.20546	Hydrophobic	Pi-Alkyl
		ALA350	4.82725	Hydrophobic	Pi-Alkyl

surface area (> 135 nm^2), suggesting greater solvent accessibility. In contrast, the native ligand reduced SASA values, reflecting deep insertion into the binding pocket. Hesperetin maintained intermediate solvent exposure, consistent with a more flexible but persistent binding interaction. Compactness alone did not correlate with higher stability, since 5,7,3′,4′-tetrahydroxyflavone displayed RMSD fluctuations despite maintaining low Rg. Conversely, hesperetin's less compact but equilibrated structure suggests adaptability within the binding site. The combined interpretation of Rg and SASA demonstrates that each ligand stabilizes ESR1 differently. These results indicate hesperetin achieves stable binding by balancing compactness with solvent exposure.

The hydrogen bonding patterns observed across 300 ns highlight distinct stabilization mechanisms among the ligands (Fig. 9). The 5,7,3′,4′-tetrahydroxyflavone formed up to four hydrogen bonds, indicating frequent and diverse interactions. The native ligand consistently maintained one to three hydrogen bonds, displaying steady anchoring. In contrast, hesperetin generally exhibited fewer interactions, typically one or two bonds at intermittent intervals. Despite lower frequency, hesperetin's interactions showed persistence, supporting stable anchoring throughout the trajectory. These results confirm that hydrogen bond count is not directly proportional to binding stability. The 5,7,3′,4′-tetrahydroxyflavone, although forming multiple bonds, still demonstrated RMSD fluctuations, reflecting compensatory interactions. The native ligand's consistent hydrogen bonds align with its naturally optimized binding. Hesperetin's fewer but more persistent hydrogen bonds emphasize the importance of quality and orientation over quantity. Such interaction patterns reveal different strategies by which ligands stabilize ESR1. Altogether, hydrogen bond dynamics suggest hesperetin employs a selective yet reliable binding mode.

Residue-specific hydrogen bond contributions were quantified, as summarized in Table 6. The 5,7,3′,4′-tetrahydroxyflavone exhibited the highest total occupancy (228.93%), dominated by GLU353 and HIS524, reflecting strong dependence on these residues. The native ligand showed moderate occupancy (122.62%), with GLU353 and HIS524 again serving as principal contributors. Hesperetin, in contrast, displayed markedly lower occupancy (24.38%), engaging residues such as CYS417, GLU353, and GLY420. Despite its reduced occupancy, hesperetin maintained stable binding throughout the simulation, emphasizing the sufficiency of selective contacts. The 5,7,3′,4′-tetrahydroxyflavone's over-reliance on GLU353 may explain its structural fluctuations in RMSD, as excessive bonding suggests compensatory rather than optimal interactions. The native ligand's balanced hydrogen bonding highlights its evolutionarily refined binding behavior. Hesperetin's selective engagement strategy reflects an efficient pharmacophoric fit within ESR1. These findings demonstrate that occupancy quantity does not equate to stability or binding efficiency. Taken together, hydrogen bond occupancy analysis reinforces hesperetin's ability to sustain ESR1 stability through strategic residue interactions.

3.9. Binding free energy analysis using MM-PBSA

The MM-PBSA analysis provided quantitative insight into the thermodynamic contributions underlying ESR1–ligand interactions (Table 7). The 5,7,3′,4′-tetrahydroxyflavone complex demonstrated the most favorable binding free energy with a ΔTOTAL of −79.695 kJ/mol, strongly supported by van der Waals forces (ΔEVDW = −103.460 kJ/mol) and electrostatic energy (ΔEEEL = −81.418 kJ/mol). These negative values indicate that both hydrophobic packing and polar interactions played a major role in stabilizing the 5,7,3′,4′-tetrahydroxyflavone complex. The native ligand followed with a ΔTOTAL of −72.521 kJ/mol, driven by a large van der Waals contribution (−110.764 kJ/mol) combined with moderate electrostatic stabilization (−25.544 kJ/mol). However, its polar solvation energy (ΔEGB = 74.583 kJ/mol) acted as a destabilizing factor, partially offsetting the favorable interactions. Surface energies (ΔESURF) remained relatively small for both ligands, suggesting minimal additional stabilization from non-polar solvation. These findings suggest that the strong electrostatic and hydrophobic forces of 5,7,3′,4′-tetrahydroxyflavone contribute to its superior affinity. By comparison, the native ligand showed a more balanced but slightly weaker energetic profile, consistent with its role as an optimized natural binder.

Hesperetin exhibited the weakest binding free energy among the three ligands, with a ΔTOTAL of −55.737 kJ/mol, reflecting reduced stabilizing contributions. Its van der Waals component (ΔEVDW = −90.389 kJ/mol) and electrostatic energy (ΔEEEL = −12.952 kJ/mol) were markedly smaller than those of 5,7,3′,4′-tetrahydroxyflavone and

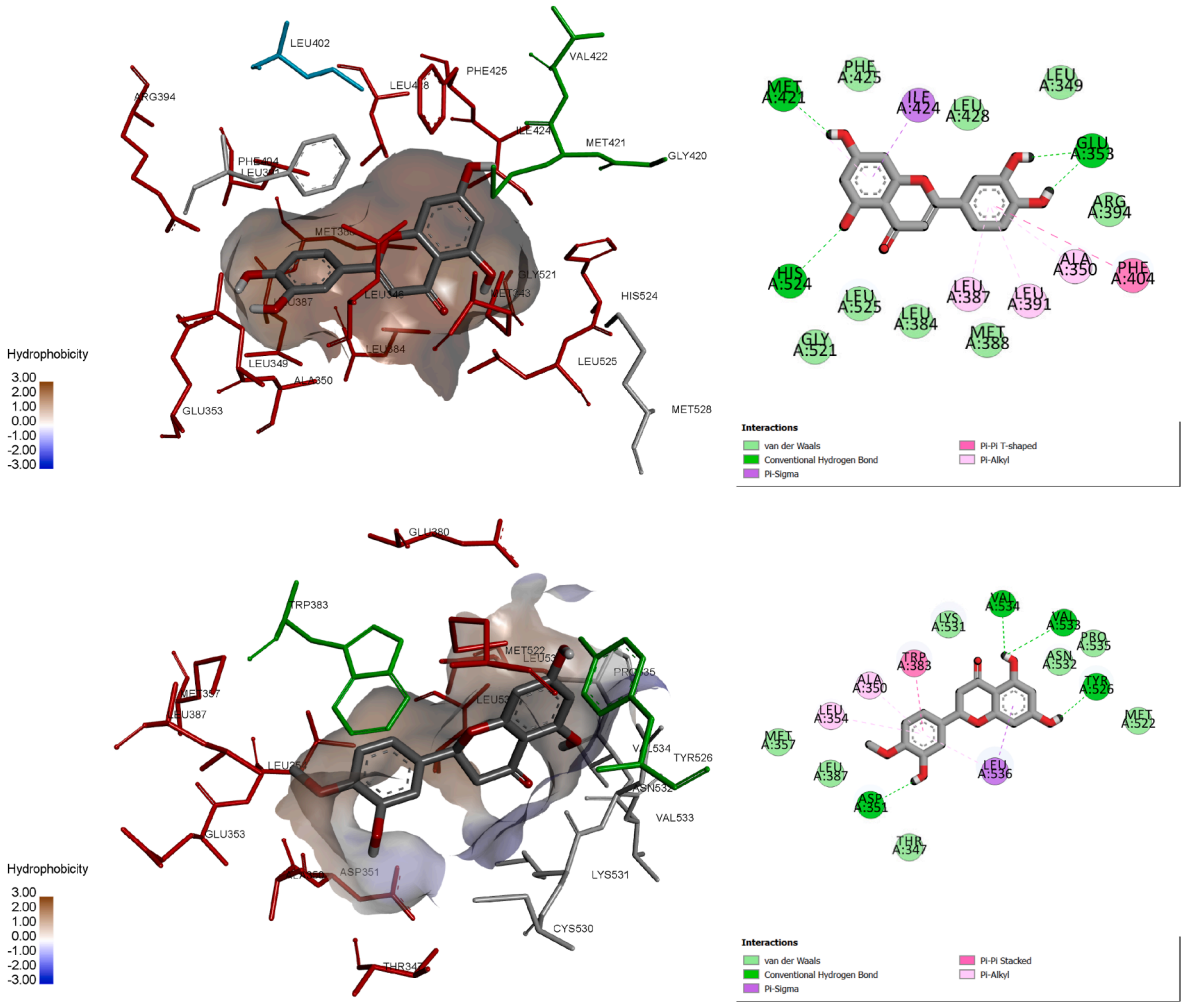


Fig. 5. Molecular docking interaction of 5,7,3′,4′-Tetrahydroxyflavone (top) and hesperetin (bottom) with ESR1.

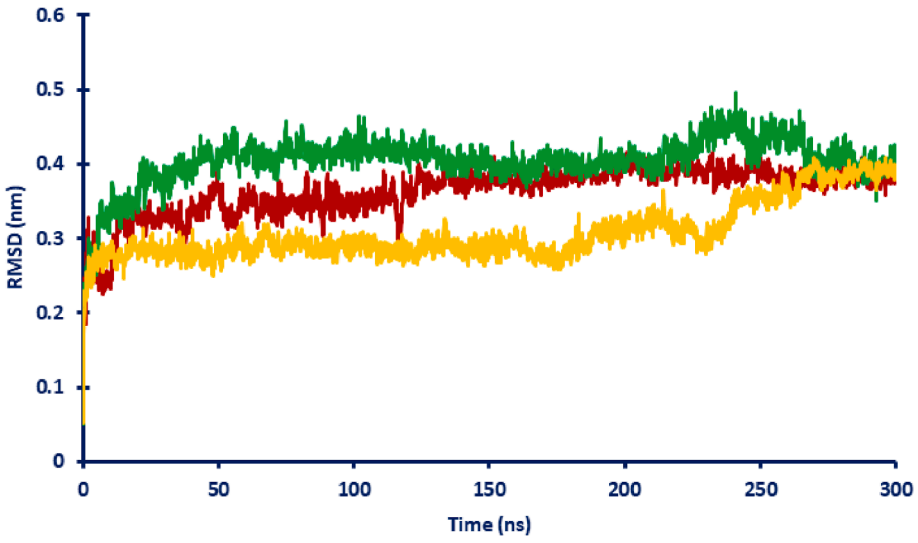


Fig. 6. The RMSD plots for the complexes of ESR1 with native ligand (compound 19) (red), 5,7,3′,4′-Tetrahydroxyflavone (yellow), and hesperetin (green).

the native ligand. Despite this, hesperetin still produced a negative overall free energy, confirming that binding to ESR1 remains thermodynamically favorable. The solvation penalty (ΔEGB = 56.277 kJ/mol) was smaller compared to the other ligands, yet not sufficient to compensate for weaker attractive forces. These results suggest that hesperetin interacts with ESR1 through fewer stabilizing contacts but maintains binding stability, as supported by MD trajectories. The relatively small differences between the native ligand and 5,7,3′,4′-

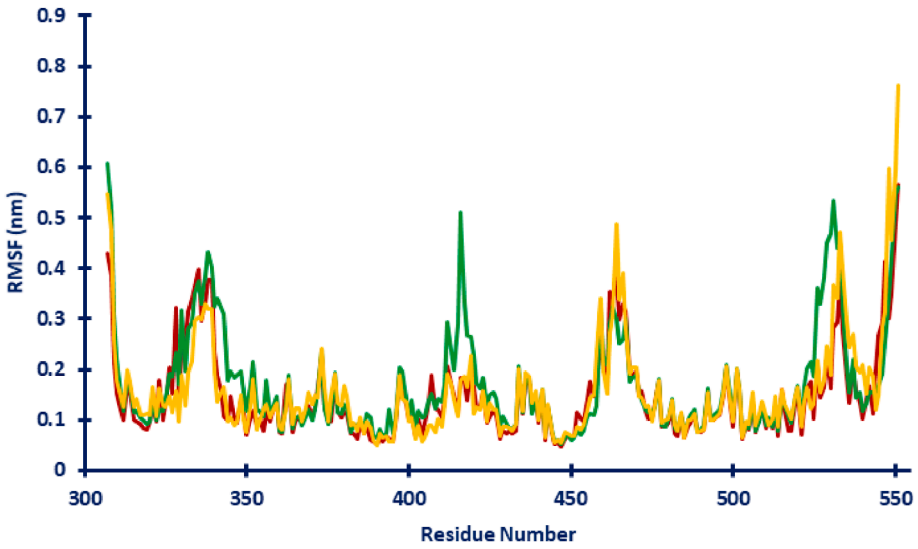


Fig. 7. The RMSF plots for the complexes of ESR1 with native ligand (compound 19) (red), 5,7,3′,4′-Tetrahydroxyflavone (yellow), and hesperetin (green).

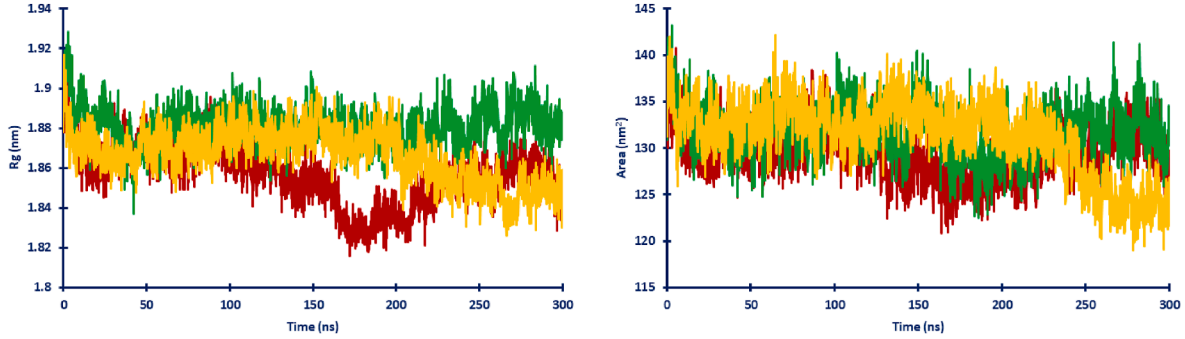


Fig. 8. The Rg (left) and SASA (right) plots for the complexes of ESR1 with native ligand (compound 19) (red), 5,7,3′,4′-Tetrahydroxyflavone (yellow), and hesperetin (green).

tetrahydroxyflavone imply that both form strong complexes, while hesperetin stabilizes ESR1 less efficiently. Importantly, the integration of MM-PBSA with dynamic results reinforces that hesperetin's stability derives more from selective residue interactions than from strong energetic contributions. Thus, MM-PBSA clarifies the energetic foundations behind the observed structural and dynamic stability of ESR1–ligand complexes.

4. Discussion

Estrogen receptor 1 (ESR1) is a vital molecular target in estrogen-dependent breast cancer due to its central role in regulating cell proliferation and survival. The selective binding of 24 metabolites from *Citrus aurantium* to ESR1, as opposed to the 111 compounds initially screened, indicates strong structural compatibility. This selectivity is particularly evident among flavonoids and methoxylated compounds which often share core features with endogenous estrogens. These features include planar aromatic rings and hydroxyl substitutions that enable hydrogen bonding and pi–pi stacking interactions. Previous studies showed that 3,5,7,4′-tetrahydroxyflavone (Kaempferol), a structurally similar flavonoid, inhibited ESR1-positive breast cancer cell growth.[51–53] The presence of similar chemical scaffolds in *Citrus* compounds suggests potential as selective estrogen receptor modulators. Such natural SERMs are of interest due to their dual agonist–antagonist activity with fewer adverse effects. The pharmacophore alignment with the ESR1 binding pocket explains their prioritization for docking and dynamic simulations. These findings demonstrate the relevance of *Citrus aurantium* as a natural source of therapeutic agents for breast cancer. Thus, the early selection step serves both as a filter and as a validation of pharmacological relevance.

Molecular docking studies revealed favorable binding affinities for 5,7,3′,4′-tetrahydroxyflavone, hesperetin, and alpha-copaene, each demonstrating consistent interactions with critical ESR1 residues such as GLU353, HIS524, and ARG394. These amino acids are essential within the ligand-binding domain and play a central role in regulating receptor activation and coactivator recruitment. The interaction profiles identified in this study are consistent with previously reported flavonoid–ESR1 complexes, where compounds established stable hydrogen bonds and hydrophobic contacts at similar residue positions. Notably, prior analyses involving structurally related flavones also described π-stacking and hydrogen bonding interactions at GLU353 and HIS524, indicating a conserved binding mode.[54,55] In the present study, 5,7,3′,4′-tetrahydroxyflavone and hesperetin exhibited superior ligand efficiency compared to alpha-copaene, underscoring the importance of hydroxyl and methoxy groups in enhancing electrostatic compatibility. These functional groups contribute to more persistent receptor engagement and greater conformational stabilization. The similarities between the current results and earlier docking investigations affirm the reliability of the docking protocol and support the predicted biological relevance of the interactions. Variability in interaction types, including both polar and nonpolar contacts, also suggests that each compound may influence ESR1 through distinct modulation mechanisms.[56] Among

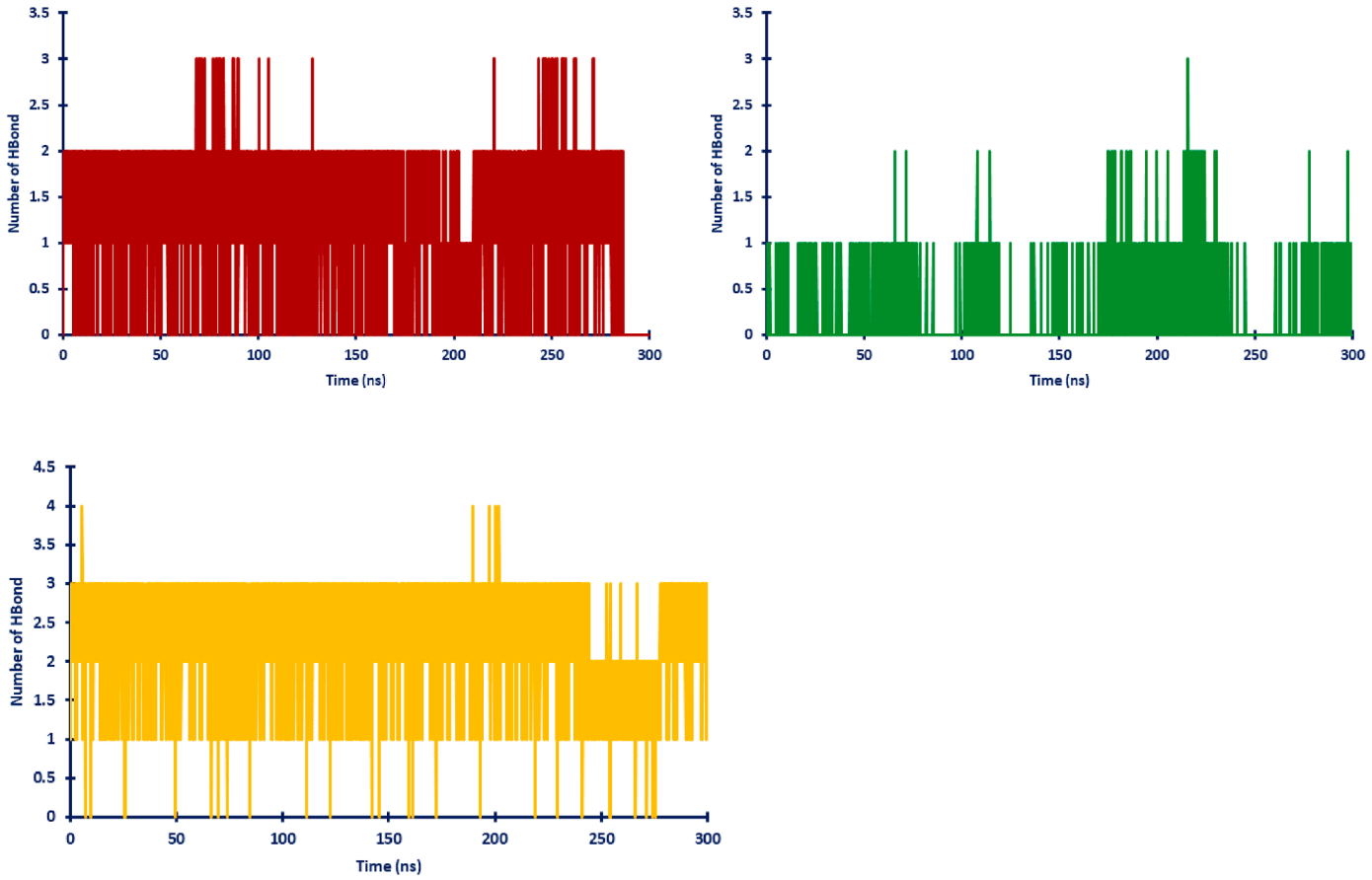


Fig. 9. The number of hydrogen bonds formed between ESR1 and native ligand (compound 19) (red), 5,7,3′,4′-Tetrahydroxyflavone (yellow), and hesperetin (green).

the tested ligands, 5,7,3′,4′-tetrahydroxyflavone displayed the deepest pocket engagement and the most stable docking conformation. By contrast, hesperetin formed fewer key interactions and was positioned more superficially within the binding site. This distinction was further confirmed by MM/PBSA calculations, which showed that the most effective ligands derived their stability primarily from van der Waals and electrostatic forces.

Molecular dynamics simulations validated the structural stability and dynamic interactions of *Citrus aurantium* metabolites with ESR1 over the 300-ns trajectory. The RMSD and RMSF analyses showed that the native ligand maintained the most consistent binding pose with minimal deviation, while 5,7,3′,4′-tetrahydroxyflavone exhibited intermediate fluctuations and hesperetin displayed higher displacements, though it equilibrated after 100 ns. Compactness and solvent accessibility analysis revealed that the native ligand complex was the most compact, tetrahydroxyflavone demonstrated greater solvent exposure, and hesperetin showed moderate structural adaptation. RDF confirmed dense atomic clustering for tetrahydroxyflavone around the receptor pocket, indicating persistent spatial occupancy. Hydrogen bond analysis indicated that tetrahydroxyflavone engaged ESR1 with the highest number and occupancy, particularly through GLU353 and HIS524, while hesperetin formed fewer but selective interactions with residues such as CYS417 and GLU353. These dynamic patterns are consistent with prior molecular dynamics reports, where stable flavonoid–receptor interactions were correlated with improved pharmacological efficacy.[57,58] This was further supported by MM-PBSA analysis, which showed 5,7,3′,4′-tetrahydroxyflavone achieving the most favorable binding free energy (−79.695 kJ/mol), followed by the native ligand (−72.521 kJ/mol), while hesperetin displayed the weakest affinity (−55.737 kJ/mol). The stronger van der Waals and electrostatic

Table 6
The hydrogen bond occupancy of ESR1 Interacting residues with native ligand (compound 19), 5,7,3′,4′-Tetrahydroxyflavone, and hesperetin.

No	Metabolite	Interacting Residue	Hydrogen Bond Occupancy	Total
1	Native (Compound 19)	GLU353	65.19%	122.62%
		HIS524	34.51%	
		ASN532	3.76%	
		ARG394	0.07%	
		LEU387	0.73%	
		GLY420	16.22%	
		GLY521	0.23%	
2	5,7,3′,4′-Tetrahydroxyflavone	GLU353	174.72%	228.93%
		HIS524	53.40%	
		THR347	0.50%	
		MET421	0.17%	
		GLY420	0.07%	
		HIS524	0.07%	
3	Hesperetin	ASP351	0.03%	24.38%
		LYS531	0.13%	
		THR347	1.70%	
		THR347	0.23%	
		LYS531	0.60%	
		CYS530	0.03%	
		LEU525	2.60%	
		ASN532	0.07%	
		ASN532	1.00%	
		TYR526	0.07%	
		HIS524	0.10%	
		GLY420	2.33%	
		GLU353	4.16%	
		LYS529	0.10%	
		CYS417	10.73%	
		PHE404	0.40%	
		LEU349	0.03%	
		CYS530	0.07%	

Table 7
The binding free energy components of ESR1 complexes with native ligand (compound 19), 5,7,3′,4′-Tetrahydroxyflavone, and hesperetin.

No	Metabolite	ΔEVDW (kJ/mol)	ΔEEEL (kJ/mol)	ΔEGB (kJ/mol)	ΔESURF (kJ/mol)	ΔGGAS (kJ/mol)	ΔGSOLV (kJ/mol)	ΔTOTAL (kJ/mol)
1	Native (Compound 19)	−110.764	−25.544	74.583	−10.796	0.000	0.000	−72.521
2	5,7,3′,4′-Tetrahydroxyflavone	−103.460	−81.418	116.994	−11.811	0.000	0.000	−79.695
3	Hesperetin	−90.389	−12.952	56.277	−8.673	0.000	0.000	−55.737

contributions in 3,5,7,4′-tetrahydroxyflavone highlight its enhanced thermodynamic stabilization, whereas hesperetin's lower values explain its reduced binding energy despite dynamic stability. Taken together, these findings suggest that 3,5,7,4′-tetrahydroxyflavone and hesperetin remain viable ESR1 binders, with the former showing superior thermodynamic favorability and the latter offering selective but stable pharmacophoric interactions.

5. Conclusions

In conclusion, this study highlighted *Citrus aurantium*-derived flavonoids as promising ESR1 modulators relevant to breast cancer therapy. Molecular dynamics analyses revealed that the native ligand maintained the most stable trajectory, 3,5,7,4′-tetrahydroxyflavone exhibited intermediate fluctuations with strong receptor engagement, and hesperetin showed higher deviations yet equilibrated after 100 ns. RMSF, Rg, and SASA analyses confirmed that tetrahydroxyflavone maintained persistent atomic clustering and solvent exposure, while hesperetin provided moderate adaptation supported by selective residue contacts. Hydrogen bond and occupancy studies showed that 3,5,7,4′-tetrahydroxyflavone engaged ESR1 through sustained interactions at GLU353 and HIS524, whereas hesperetin relied on fewer but targeted bonds at residues like CYS417 and GLU353. Importantly, MM-PBSA calculations indicated that 3,5,7,4′-tetrahydroxyflavone achieved the most favorable binding free energy (−79.695 kJ/mol), followed by the native ligand (−72.521 kJ/mol), while hesperetin displayed the weakest affinity (−55.737 kJ/mol). These results demonstrate that 3,5,7,4′-tetrahydroxyflavone benefits from strong van der Waals and electrostatic stabilization, while hesperetin achieves binding through efficient pharmacophoric fit despite weaker energetics. The hydroxyl-rich aromatic structures of both flavonoids contributed to selective ESR1 engagement, consistent with prior studies linking flavonoid–receptor stability to pharmacological potential. Together, these findings provide a solid foundation for experimental validation and future development of *Citrus aurantium* metabolites as potential therapeutic agents in estrogen receptor-positive breast cancer.

CRediT authorship contribution statement

Taufik Muhammad Fakih: Writing – review & editing, Writing – original draft, Visualization, Validation, Supervision, Software, Resources, Project administration, Methodology, Investigation, Funding acquisition, Formal analysis, Data curation, Conceptualization. **Haura Syabihah:** Visualization, Validation, Resources, Methodology, Investigation, Data curation. **Tri Awalani Sapa'ati Gusti:** Visualization, Validation, Resources, Methodology, Data curation. **Tifanil Oktafira:** Visualization, Validation, Resources, Methodology, Data curation. **Nency Oktavia Sri Mulyani:** Visualization, Validation, Resources, Methodology, Data curation. **Hilda Aprilia Wisnuwardhani:** Visualization, Validation, Software, Resources, Methodology, Investigation, Formal analysis, Data curation. **Muchtaridi Muchtaridi:** Writing – review & editing, Writing – original draft, Visualization, Validation, Supervision, Software, Resources, Project administration, Methodology, Investigation, Funding acquisition, Formal analysis, Data curation, Conceptualization.

Funding

This research received no external funding.

Declaration of competing interest

The authors declare that they have no known competing financial interests or personal relationships that could have appeared to influence the work reported in this paper.

Acknowledgment

The authors would like to express their sincere gratitude to Rector of Universitas Padjadjaran, for providing valuable support and facilities that contributed to the successful completion of this research. This publication charge is funded by Universitas Padjadjaran through the Indonesian Endowment Fund for Education (LPDP) on behalf of the Indonesian Ministry of Higher Education, Science and Technology and managed under the EQUITY Program (Contract No. 4303/B3/DT.03.08/2025 and 3927/UN6.RKT/HK.07.00/2025).

Data availability

The data supporting the findings of this study are available within publicly accessible scientific databases and literature sources, all of which are appropriately cited in the manuscript. Secondary metabolite data of *Citrus aurantium* were obtained from the KNApSAcK Family database (www.knapsackfamily.com/). Structural information of compounds, including canonical SMILES, was retrieved from PubChem (pubchem.ncbi.nlm.nih.gov/) and subsequently analyzed using SwissADME (www.swissadme.ch/) and ProTox 3.0 (tox.charite.de/protox3/#) for pharmacokinetics and toxicity profiling. Target and disease-related information were collected from GeneCards (www.genecards.org/) and SwissTargetPrediction (www.swisstargetprediction.ch/). Overlapping targets were visualized using FunRich v3.1.3, and protein–protein interaction data were acquired from STRING (string-db.org/) and analyzed in Cytoscape v3.10.3 with CytoHubba. The ESR1 protein structure (PDB ID: 1XPC) was retrieved from the Protein Data Bank (www.rcsb.org/). Docking studies were performed using AutoDock Tools 1.5.7 and AutoDock Vina, with visualization in BIOVIA Discovery Studio 2021. Molecular dynamics simulations were carried out using GROMACS 2016.3 with ligand topologies prepared by ACPYPE, and binding free energy calculations were performed using the g_mmpbsa tool. Any processed datasets, docking outputs, or MD simulation trajectories generated during this study are available from the corresponding author upon reasonable request.

References

1. Ban KA, Godellas CV. Epidemiology of breast cancer. *Surg Oncol Clin.* 2014;23.
2. Shang C, Xu D. Epidemiology of breast cancer. *Oncologie.* 2022;24.
3. Xu H, Xu B. Breast cancer: epidemiology, risk factors and screening. *Chin J Cancer Res.* 2023;35.
4. Arnold M, Morgan E, Rumgay H, et al. Current and future burden of breast cancer: global statistics for 2020 and 2040. *Breast.* 2022;66.

5. Alexandraki A, Papageorgiou E, Zacharia M, et al. New insights in the era of clinical biomarkers as potential predictors of systemic therapy-induced cardiotoxicity in women with breast cancer: a systematic review. *Cancers*. 2023;15.
6. Fan L, Goss PE, Strasser-Weippl K. Current status and future projections of breast cancer in Asia. *Breast Care*. 2015;10.
7. Mirza MR, Lorusso D, Shen Q, et al. First-line treatments for advanced or recurrent endometrial cancer: systematic literature review of clinical evidence. *Crit Rev Oncol Hematol*. 2025;206:104555.
8. Cucciniello L, Garufi G, Di Rienzo R, et al. Estrogen deprivation effects of endocrine therapy in breast cancer patients: incidence, management and outcome. *Cancer Treat Rev*. 2023;120.
9. Meiyanto E, Larasati YA. The chemopreventive activity of Indonesia medicinal plants targeting on hallmarks of cancer. *Adv Pharmaceut Bull*. 2019;9.
10. Cahyaningsih R, Phillips J, Magos Brehm J, Gaisberger H, Maxted N. Climate change impact on medicinal plants in Indonesia. *Glob Ecol Conserv*. 2021;30.
11. Rahayu YYS, Sujarwo W, Irsyam ASD, Dwiartama A, Rosleine D. Exploring unconventional food plants used by local communities in a rural area of West Java, Indonesia: ethnobotanical assessment, use trends, and potential for improved nutrition. *J Ethnobiol Ethnomed*. 2024;20:1–23.
12. Yin SY, Wei WC, Jian FY, Yang NS. Therapeutic applications of herbal medicines for cancer patients. *Evid base Compl Alternative Med*. 2013, 2013.
13. Guo M, Qin S, Wang S, et al. Herbal medicine nanocrystals: a potential novel therapeutic strategy. *Molecules*. 2023;28.
14. Pirintsos S, Panagiotopoulos A, Bariotakis M, et al. From traditional ethnopharmacology to modern natural drug discovery: a methodology discussion and specific examples. *Molecules*. 2022;27.
15. Seyyedi-Mansour S, Donn P, Barciela P, et al. Citrus aurantium flowers: overview of chemistry, functionality, and technological applications. *Molecules*. 2025;30.
16. Langgut D. The citrus route revealed: from southeast Asia into the Mediterranean. *Hortscience*. 2017;52.
17. Fernández-Cabal J, Avilés-Betanzos KA, Cauich-Rodríguez JV, Ramírez-Sucre MO, Rodríguez-Buenfil IM. Recent developments in citrus aurantium L.: an overview of bioactive compounds, extraction techniques, and technological applications. *Processes*. 2025;13.
18. Suntar I, Khan H, Patel S, Celano R, Rastrelli L. An overview on citrus aurantium L.: its functions as food ingredient and therapeutic agent. *Oxid Med Cell Longev*. 2018, 2018.
19. Chen Q, Wang D, Tan C, Hu Y, Sundararajan B, Zhou Z. Profiling of flavonoid and antioxidant activity of fruit tissues from 27 Chinese local citrus cultivars. *Plants*. 2020;9.
20. Segun PA, Ismail FMD, Ogbole OO, et al. Acridone alkaloids from the stem bark of Citrus aurantium display selective cytotoxicity against breast, liver, lung and prostate human carcinoma cells. *J Ethnopharmacol*. 2018;227.
21. Wang ZY, Wang X, Zhang DY, Hu YJ, Li S. Traditional Chinese medicine network pharmacology: development in new era under guidance of network pharmacology evaluation method guidance. *Zhongguo Zhongyao Zazhi*. 2022;47.
22. Zhang P, Zhang D, Zhou W, et al. Network pharmacology: towards the artificial intelligence-based precision traditional Chinese medicine. *Briefings Bioinf*. 2024;25.
23. Thakur C, Qiu Y, Fu Y, et al. Epigenetics and environment in breast cancer: new paradigms for anti-cancer therapies. *Front Oncol*. 2022;12.
24. Noor F, Qamar MTU, Ashfaq UA, Albutti A, Alwashmi ASS, Aljasir MA. Network pharmacology approach for medicinal plants: review and assessment. *Pharmaceuticals*. 2022;15.
25. Afendi FM, Okada T, Yamazaki M, et al. KNApSAcK family databases: integrated metabolite-plant species databases for multifaceted plant research. *Plant Cell Physiol*. 2012;53:e1.
26. Daina A, Michielin O, Zoete V. SwissADME: a free web tool to evaluate pharmacokinetics, drug-likeness and medicinal chemistry friendliness of small molecules. *Sci Rep*. 2017;7.
27. Banerjee P, Eckert AO, Schrey AK, Preissner R. ProTox-II: a webserver for the prediction of toxicity of chemicals. *Nucleic Acids Res*. 2018;46.
28. Safran M, Rosen N, BarShir R, et al. *GeneCards – the human gene database. The GeneCards Suite chapter. Practical Guide to Life Science Databases*. 2022.
29. Gfeller D, Grosdidier A, Wirth M, Daina A, Michielin O, Zoete V. SwissTargetPrediction: a web server for target prediction of bioactive small molecules. *Nucleic Acids Res*. 2014;42.
30. Szklarczyk D, Nastou K, Koutrouli M, et al. The STRING database in 2025: protein networks with directionality of regulation. *Nucleic Acids Res*. 2025;53:D730–D737.
31. Shannon P, Markiel A, Ozier O, et al. Cytoscape: a software environment for integrated models of biomolecular interaction networks. *Genome Res*. 2003;13.
32. Morris G, Huey R, Lindstrom W, Sanner M, Belew R, Goodsell D. AutoDock 4 and AutoDock tools 4: automated docking with selective receptor flexibility. *J Compitation Chem*. 2009;30:2785–2791.
33. Eberhardt J, Santos-Martins D, Tillack AF, Forli S. AutoDock Vina 1.2.0: new docking methods, expanded force field, and python bindings. *J Chem Inf Model*. 2021;61.
34. BIOVIA. *Dassault Systèmes BIOVIA, Discovery Studio Modeling Environment, Release 2017*. San Diego: Dassault Systèmes; 2017.
35. Kim S, Chen J, Cheng T, et al. PubChem 2023 update. *Nucleic Acids Res*. 2023;51.
36. Blizzard TA, Dininno F, Morgan JD, et al. Estrogen receptor ligands. Part 9: dihydrobenzoxathiin SERAMs with alkyl substituted pyrrolidine side chains and linkers. *Bioorg Med Chem Lett*. 2005;15.
37. Abraham MJ, Murtola T, Schulz R, et al. GROMACS: high performance molecular simulations through multi-level parallelism from laptops to supercomputers. *SoftwareX*. 2015;1–2:19–25.
38. Sousa da Silva AW, Vranken WF. ACPYPE - AnteChamber PYthon parser interfacE. *BMC Res Notes*. 2012;5:367.
39. Kumari R, Kumar R, Consortium OSDD, Lynn A. g _ mmpbsa - a GROMACS tool for MM-PBSA and its optimization for high-throughput binding energy calculations. *J Chem Inf Model*. 2014.
40. Karami TK, Hailu S, Feng S, Graham R, Gukasyan HJ. Eyes on Lipinski's rule of five: a new "Rule of Thumb" for physicochemical design space of ophthalmic drugs. *J Ocul Pharmacol Therapeut*. 2022;38.
41. Setlur AS, Karunakaran C, Panhalkar V, Sharma S, Sarkar M, Niranjan V. Multifaceted computational profiling of thymol and geraniol against the human proteome for bio-repellent alternatives: toxicity predictions, degradation analysis, and quantum mechanical approaches. *Acta Trop*. 2024;258:107359.
42. Feitelson MA, Arzumanyan A, Kulathinal RJ, et al. *Sustained proliferation in cancer: mechanisms and novel therapeutic targets*. In: *Seminars in Cancer Biology*. vol. 35. 2015.
43. Carrington EM, Zhan Y, Brady JL, et al. Anti-apoptotic proteins BCL-2, MCL-1 and A1 summate collectively to maintain survival of immune cell populations both in vitro and *in vivo*. *Cell Death Differ*. 2017;24.
44. Asghar U, Witkiewicz AK, Turner NC, Knudsen ES. The history and future of targeting cyclin-dependent kinases in cancer therapy. *Nat Rev Drug Discov*. 2015;14.
45. Pópulo H, Lopes JM, Soares P. The mTOR signalling pathway in human cancer. *Int J Mol Sci*. 2012;13.
46. Shi D, Gu W. Dual roles of MDM2 in the regulation of p53: ubiquitination dependent and ubiquitination independent mechanisms of MDM2 repression of p53 activity. *Genes Cancer*. 2012;3.
47. You CP, Leung MH, Tsang WC, Khoo US, Tsoi H. Androgen receptor as an emerging feasible biomarker for breast cancer. *Biomolecules*. 2022;12.
48. Kamel EM, Aba Alkhayl FF, Alqhtani HA, Bin-Jumah M, Lamsabhi AM. Dynamic interactions and inhibitory mechanisms of Artemisia annua terpenoids with carbonic anhydrase IX. *Int J Biol Macromol*. 2024;282:136982.
49. Liu B, Peng Z, Zhang H, et al. Regulation of cellular senescence in tumor progression and therapeutic targeting: mechanisms and pathways. *Mol Cancer*. 2025;24.
50. Clusan L, Ferrière F, Flouriot G, Pakdel F. A basic review on estrogen receptor signaling pathways in breast cancer. *Int J Mol Sci*. 2023;24.
51. Rhazri K, Hamri S, Lebri M, et al. Isolation of 3,5,7,4'-Tetrahydroxyflavone (Kaempferol) from the methanol extract of the leaves of Cassia Alata and in-vitro evaluation of its potential inhibitory effect on the human Pulmonary Arterial Hypertension (PAH). *Der Pharma Chemica*. 2015;7.
52. Wang X, Yang Y, An Y, Fang G. The mechanism of anticancer action and potential clinical use of kaempferol in the treatment of breast cancer. *Biomed Pharmacother*. 2019;117.
53. Widyananda MH, Fatchiyah F, Muflikhah L, Ulfa SM, Widodo N. Computational examination to reveal Kaempferol as the most potent active compound from Euphorbia hirta against breast cancer by targeting AKT1 and ERα. *Egyptian J Basic Appl Sci*. 2023;10.
54. Ng HW, Zhang W, Shu M, et al. Competitive molecular docking approach for predicting estrogen receptor subtype α agonists and antagonists. *BMC Bioinf*. 2014;15:1–15.
55. Fang S, Su H, Liu J, et al. Network pharmacology and molecular docking to explore the potential mechanism of chlorogenic acid in septic acute liver injury and experimental validation of TLR4/NF-κB pathway *in vivo*. *Naunyn-Schmiedebergs Arch Pharmacol*. 2025;398:7331–7342.
56. Zhang S, Yang Y, Zhang R, et al. The potential mechanism of alpiniae oxyphyllae fructus against hyperuricemia: an integration of network pharmacology, molecular docking, molecular dynamics simulation, and in vitro experiments. *Nutrients*. 2025;17.
57. Alhadrami HA, Sayed AM, Hassan HM, Alhadrami AH, Rateb ME. Molecular insights and inhibitory dynamics of flavonoids in targeting Pim-1 kinase for cancer therapy. *Front Pharmacol*. 2024;15:1–15.
58. Fegade BS, Chaudhari SY, Likhar RV, et al. Design, synthesis, molecular docking and molecular dynamics studies of some 3-methoxy flavone derivatives as an anti-breast cancer agent. *Discov Oncol*. 2025;16.